Assessment of subgrid-scale models with an LES-dedicated experimental database: the pulsatile impinging jet in turbulent cross-flow

Hubert Baya Toda,[1, a)] Olivier Cabrit,[2, 3] Karine Truffin,[1] Gilles Bruneaux,[1] and Franck Nicoud[4]

[1)] *IFP Energies nouvelles, 1 & 4 avenue de Bois-Preau, 92852 Rueil-Malmaison, France*

[2)] *CERFACS, 42 avenue Gaspard Coriolis, 31057 Toulouse Cedex 01, France*

[3)] *Department of Mechanical Engineering, University of Melbourne, Victoria 3010, Australia*

[4)] *Université Montpellier 2, UMR CNRS 5149 / CC51, Place Eugène Bataillon, 34095 Montpellier, France*

(Dated: 6 July 2014)

Large-Eddy Simulation (LES) in complex geometries and industrial applications like piston engines, gas turbines or aircraft engines requires the use of advanced subgrid-scale (SGS) models able to take into account the main flow features and the turbulence anisotropy. Keeping this goal in mind, this paper reports an LES-dedicated experiment of a pulsatile hot-jet impinging a flat-plate in the presence of a cold turbulent cross-flow. Unlike commonly used academic test cases, this configuration involves different flow features encountered in complex configurations: shear/rotating regions, stagnation point, wall-turbulence, and the propagation of a vortex ring along the wall. This experiment was also designed with the aim to use quantitative and nonintrusive optical diagnostics such as Particle Image Velocimetry (PIV), and to easily perform an LES involving a relatively simple geometry and well-controlled boundary conditions. Hence, two eddy-viscosity-based SGS models are investigated: the dynamic Smagorinsky model[1] and the σ-model[2]. Both models give similar results during the first phase of the experiment. However, it was found that the dynamic Smagorinsky model could not accurately predict the vortex-ring propagation, while the σ-model provides a better agreement with the experimental measurements. Setting aside the implementation of the dynamic procedure (implemented here in its simplest form, *i.e.* without averaging over homogeneous directions and with clipping of negative values to ensure numerical stability), it is suggested that the mitigated predictions of the dynamic Smagorinsky model are due to the dynamic constant, which strongly depends on the mesh resolution. Indeed, the shear-stress near the wall increases during the vortex-ring impingement leading to a less refined mesh in terms of wall units, y^+. This loss of resolution induces a poor damping of the dynamic constant, which is no longer able to adjust itself to ensure the expected y^3-behaviour near the wall. It is shown that the dynamic constant is never small enough to properly balance the large values of the squared magnitude of the strain-rate tensor, $2S_{ij}S_{ij}$. The experimental database is made available to the community upon request to the authors.

[a)]Corresponding author.; Electronic mail: hubert.baya-toda@ifpen.fr

I. INTRODUCTION

The ever increasing capability of supercomputers is currently paving the way for Large-Eddy Simulation (LES) in complex geometries. Since the pioneering work of Smagorinsky[3], numerous subgrid-scale (SGS) viscosity models[1,4–6] were developed, but their extension to complex geometries remains an open question. This is notably the case for the well-known dynamic Smagorinsky model[1] for which the flow complexity may limit the possibility of averaging over homogeneous directions. For instance, in Internal Combustion engines (IC engines) many physical mechanisms interact in a time-varying geometry: combustion, spray atomization, multiphase flows, heat transfer, wall interaction, etc. This is illustrated in Fig. 1 for a diesel jet combustion.

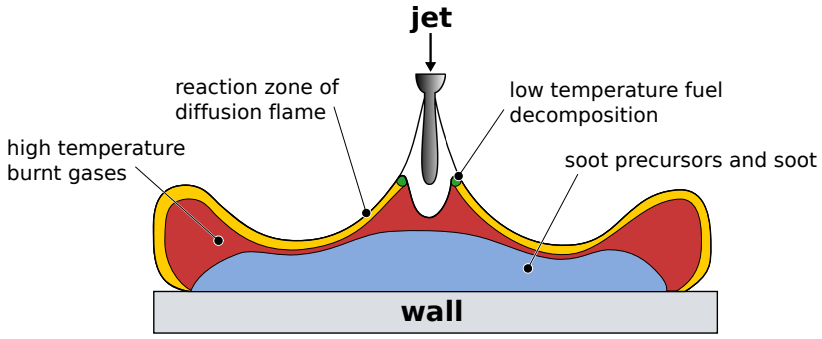

FIG. 1. Schematic diagram of a diesel jet impinging a wall in an internal combustion engine[7].

Although different improvements[8–10] of the dynamic Smagorinsky model have been proposed, the lack of detailed and relevant experimental data dedicated to complex flows restricts the assessment of SGS models to academic test cases. Homogeneous isotropic turbulence[11,12] is certainly very suitable for testing the dissipative behaviour of SGS models[2,5,10] but the turbulence state in complex configurations is neither homogeneous nor isotropic. The turbulent wall-bounded flow configuration[13–15] is a more evolved academic case which can be used to assess the near-wall behaviour of the SGS models and their ability to predict the laminar-to-turbulent transition near solid boundaries[16–22]. Unfortunately, boundary layers in industrial applications are seldom established and often disturbed by the external flow. Other interesting test cases[23–26] are available but in general are not sufficiently challenging to ensure a complete validation of the SGS models in complex geometries. If one wants to improve the use of LES for IC engines, there is thus a need

to develop cases of validation which stay as close to an engine environment as possible. However, despite the recent progress made in the field of nonintrusive optical diagnostics, a complete experimental validation in the genuine engine environment still remains a real challenge. In addition, the computation of the full engine remains very demanding in terms of computational resources[27], for both the Central Processing Unit (CPU) and the memory capacity. As a consequence, developing simple, well-controlled experiments mimicking some flow characteristics of the IC engines would be useful.

In this framework, a high-fidelity validation-platform is proposed in this paper. The purpose is to reproduce some of the typical phenomena encountered in IC engines in a relatively simple configuration; simple enough to set up a well-controlled experiment whose geometry and boundary conditions can be easily reproduced in a numerical simulation, but complex enough to exhibit the important flow features commonly observed in IC engines. A pulsatile hot-jet impinging a flat-plate in the presence of a cold turbulent cross-flow was chosen because this configuration leads to the formation of a hot vortex-ring followed by its impingement and propagation along a solid surface. Particle Image Velocimetry (PIV) was used for measuring the velocity field, and LES of the same experiment was performed. The objective of this work is twofold. First, to provide an experimental database for the validation of physical/numerical models. Second, to assess the performances of two SGS models already validated against academic test cases: the dynamic Smagorinsky model[1] and the σ-model[2]. These two models were selected because they both account for solid boundaries and vanish in various laminar flow configurations (pure shear, pure rotation, pure dilatation); the dynamic Smagorinsky model through the dynamic procedure and the σ-model through an advanced formulation of its time-scale operator.

The experimental apparatus is first described in section II. Particular emphasis is given to explain the compromises made in order to respect the constraint of performing a full size LES while using a sufficiently large experimental working-section to allow the use of optical diagnostics. Note also that it was decided not to linger on the details concerning the temperature measurements since the present study only focusses on the velocity field. Section III presents the two SGS models and the simulation parameters. In section IV, the PIV/LES comparison of the velocity field is provided, followed by a discussion in section V about the differences observed between the two SGS models. Finally, a general conclusion

is given in the last section.

II. EXPERIMENTAL APPARATUS

In IC engines and especially diesel engines, one of the most important aerothermal flow features encountered is the interaction between the fuel jet and the piston head as shown in Fig. 1. As a consequence, the main objective during the design of the experiment was to reproduce this feature in a simple way. The actual engine configuration was simplified and reduced to a non-reactive pulsatile-jet that impinges a flat surface within a turbulent cross-flow. The constraints explained in the following section led to the experimental set-up shown in Figs. 2-4.

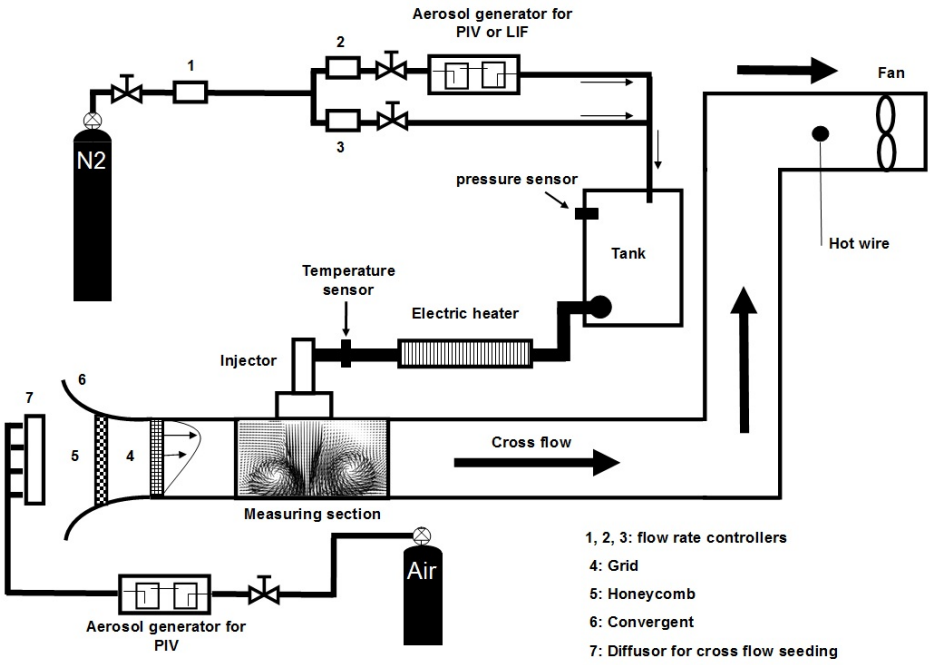

FIG. 2. Schematic of the experimental set-up.

A. Design guidelines

Particular attention was paid during the entire design development phase to the dimensions of the working-section so that they would be sufficiently large to facilitate the optical measurements while remaining small enough to be computed by a wall-resolved LES with reasonable computational resources. This led to the guidelines listed hereafter.

- **Dimensions and unsteadiness:** the distance from the injector exit to the impinging wall (channel height) was set to $H = 2D$ (where D is the injector diameter) in order to minimize the number of grid points during the computation. Such a distance is sufficient to observe the formation of the vortex-ring[28–30]. For optical accessibility purposes, the channel height was set to $H = 20\ mm$ leading to $D = 10\ mm$. Note that the nozzle hole diameter of typical IC engine injectors is of the order of 1 mm, far too small and impractical for high-fidelity optical diagnostics. For these reasons, an Hoerbiger GV 50 injector was chosen. It is characterized by a fast response time (100 μs, which is consistent with an IC engine's injector response time) and a large outflow diameter of 30 mm. This dimension was reduced to 10 mm by using a convergent volume as shown in Fig. 3.

- **Flow regime:** most of the SGS viscosity models are developed in the framework of incompressible flows and are further extended to compressible flows[31] under a low-Mach-number assumption. This means that the Mach number, M, must stay in the subsonic regime, *i.e.* $M \leq 0.2$. In the present case, this corresponds to a maximum velocity of 90 m/s. Since the maximum velocity in the experiment is controlled by the relative pressure in the tank (see Fig. 2), some preliminary PIV measurements were performed and revealed that a tank pressure of $P_{\text{tank}} = 20\ kPa$ was suitable for constraining the flow in the subsonic regime. More details about these preliminary PIV measurements are given in section II C.

- **Cross-flow:** the presence of the air cross-flow at ambient pressure and temperature was necessary to recreate a wall-bounded turbulent environment. The velocity of the cross flow was monitored with a hot wire and tuned in order to generate a significant deviation of the jet, at least of the order of one jet diameter. This was done using Schlieren visualization (not shown here) at different flow rates. The Reynolds number of the cross flow is around $Re_{\text{cross-flow}} \approx 16000$ (based on the maximum velocity and the channel height, H). The turbulent intensity of the cross flow was generated thanks to a grid situated $10D$ upstream of the jet inlet. The grid characteristics are provided in section II B.

- **Optical accessibility:** The experimental set-up was equipped with four wide optical accesses (UV-quality quartz windows - Excimer 248 nm), two on each lateral wall, one

perpendicular to the cross flow, and another on the top wall (see Figs. 3 and 4).

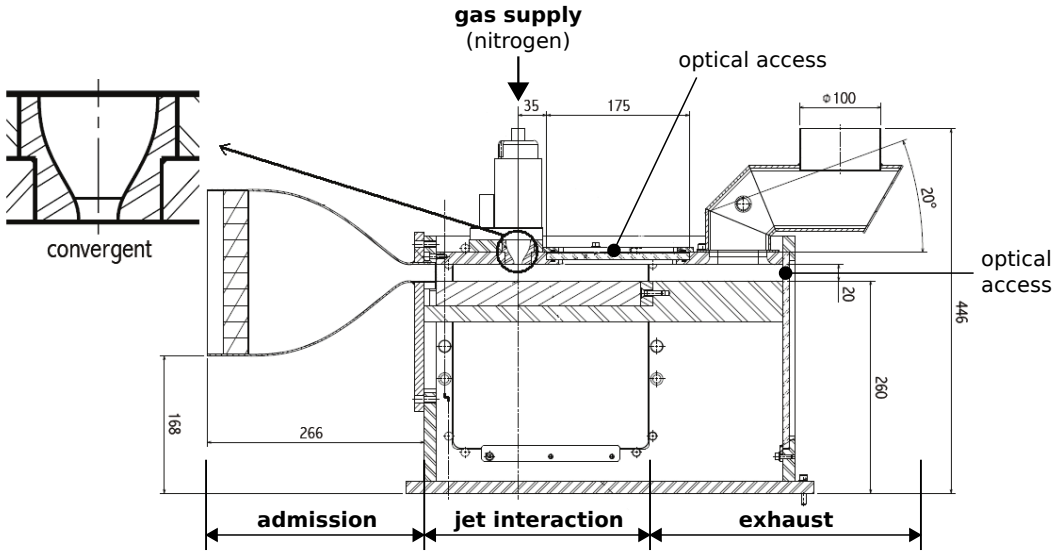

FIG. 3. Design of the experimental apparatus with a close-up view of the injector geometry (dimensions shown in millimeters).

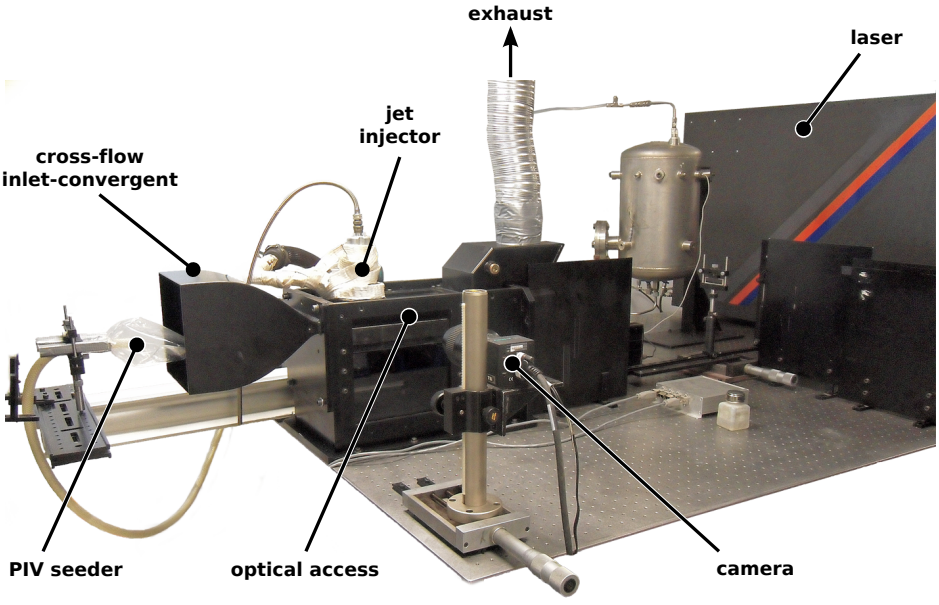

FIG. 4. Experimental apparatus with the PIV system.

B. Description of the experimental apparatus

Respecting the aforementioned guidelines, the dimensions of the experimental apparatus are shown in Fig. 3, and a photograph of the experimental bench is proposed in Fig. 4. Four main sections can be distinguished in Fig. 3: the admission, the jet-interaction, the gas supply, and the exhaust. The description of each part is provided hereafter.

- **Admission**: the aim of the admission section is to generate a turbulent wall-bounded cross-flow. It also prevents the accumulation of seeding-particles introduced for PIV in the working-section. The admission is composed of a large convergent volume for accelerating the flow, which is designed to avoid boundary layer separation[32–34]. Moreover, a honeycomb is positioned at the inlet in order to homogenise the flow and break the large-scale turbulent structures. The thickness of the honeycomb is such that it is eight times bigger than the diameter of a single cell[35]. Finally, a grid is used for imposing the turbulent intensity. It is made of circular shaped holes whose diameter increases from bottom to top (diameters ranging from $\phi_{\text{small}} = 0.5\ mm$ to $\phi_{\text{big}} = 0.8\ mm$). This diameter variation was used in order to reduce the impact of the cross-flow on the vortex ring propagation along the wall, while sufficiently deviating the jet. The distance between two consecutive holes being around $d = 0.2\ mm$, which gives a grid mesh size of $M = \phi_{\text{big}} + d = 1\ mm$ for the biggest holes. The solidity factor is around 0.5.

- **Jet-interaction:** the jet, the cross flow, and the wall all interact in this region. The injector is situated 100 mm ($100M$) downstream of the grid, which is considered far enough for the turbulence to be fully developed under the injector. The dimension of the working-section in the spanwise direction is 400 mm (200 mm from the jet centre to the edges in each direction), which corresponds to $40D$ and avoids any lateral-wall effects on the expansion of the vortex-ring after the impingement.

- **Gas supply:** the gas supply was equipped with a seeding system, and nitrogen is used as a carrier gas for the injection. In order to have regular pulsatile gas injections, a buffer volume (the tank in Fig. 2) is mounted between the nitrogen source and the injector. The volume of the tank is sufficiently large (20 L) to prevent the tank pressure from any effect of the repeated injections.

- **Exhaust:** a fan was used in the exhaust section to drive the cross flow. The corresponding flow rate, around 96 m^3/h, was estimated thanks to the hot-wire displayed in Fig. 2. This hot-wire only provided a local velocity, but it was an important component of the experimental bench in order to ensure that the measurements were always performed under the same cross-flow conditions.

C. Experimental set-up for PIV measurements

The experimental set-up for the PIV measurements is presented in Fig. 5. The laser sheet was generated by a double pulse Nd:YAG-laser (Spectra Physics reference: PIV400) working at its second harmonic, 532 nm. The time duration between two consecutive pulses was 2 μs. The frequency of the laser was 10 Hz but an external synchronizer was used in order to set the recording frequency to 1 Hz, which corresponds to the frequency of the injector pulsation. The laser sheet was generated by a combination of a divergent cylindrical lens (focal length: 40 mm) and a convergent spherical lens (focal length: 1000 mm). Different mirrors reflecting at 532 nm were used to position the laser sheet on the different planes of interest. The width of the laser sheet was about 1.5 mm and its height about 40 mm.

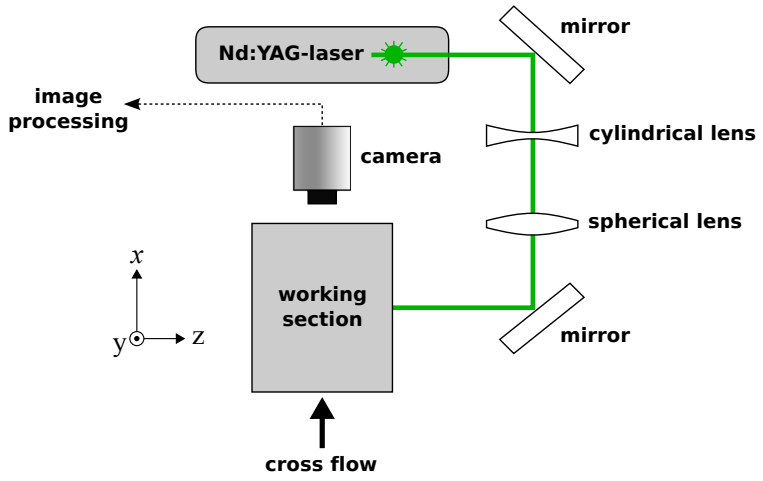

FIG. 5. Schematic of the PIV system.

The Mie scattering signal originating from the particles was collected with a CCD camera with a resolution of 2048×2048 pixels. The camera lens had a focal length of $f = 105$ mm and an aperture of $f_\sharp = 2.8$. The processing of the data was performed with the Insight 3G software. Each pair of images was processed using cross correlation based on Fast

Fourier Transformation. The size of the interrogation windows varied from 16×16 pixels to 64×64 pixels depending on the flow velocity. A local post-processing procedure based on the comparison of the velocity magnitude of the pixel of interest and the median value of the surrounding pixels was used to remove the data whose uncertainty was too high. No replacement of the removed velocity vectors was applied.

The flow was seeded with liquid particles of sebacat oil smaller than 5 μm. The Stokes number is rather small and varies between 0.05 (at late stages) and 0.15 (at early stages). The Kolmogorov scale (for the Stokes number of the seeding particles) was estimated based on the Reynolds number and the integral length estimated as equal to the injector diameter $\eta = \frac{D}{Re^{3/4}}$. At early injection timing $Re \approx 47000$ and at late timings $Re \approx 7000$. This leads to a Kolmogorov length scale which varies between $3\mu m$ and $13\mu m$. However, the pixel resolution of the camera was limited to approximately 1 mm, 300 times larger than the Kolmogorov length-scale. Consequently, the smallest scales are naturally filtered out by the acquisition system. Nevertheless, this study mainly focuses on the large-scale motion resolved by the LES, and the camera resolution and Stokes number of the particles were sufficient to measure the largest scales with a good level of fidelity. Hence, the experimental and numerical results can be compared with a good degree of confidence.

Concerning the flow seeder, two different seeding systems were used, but not simultaneously. When the jet properties were preliminary investigated without the presence of the cross-flow, the flow was seeded directly from the injector. This jet characterization was used to properly determine the jet-inlet boundary condition, and to verify that setting the relative tank pressure to $P_{\text{tank}} = 20\ kPa$ was suitable for constraining the flow in the subsonic regime. This is shown in Fig. 6, in which the maximum velocity magnitude does not exceed 90 m/s. For the pulsatile jet in cross-flow measurements, the seeding strategy was changed, and the flow was only seeded through the cross-flow as shown in Fig. 4. This could potentially lead to a loss of the measurement accuracy, but the Mie scattering signal and the particle density were found to be sufficient, even when the jet interacts with the cross-flow. Moreover, the post-processing method involved 400 individual snapshots for one given time, and the final vector (mean and standard deviation) was considered valid only if at least 80 individual vectors were properly measured. Overall, 90% of the vectors were averaged on more than 300 snapshots. It is also important to mention that comparisons between simulations and experiments in the jet in cross flow configuration were performed

at a distance greater than 2 mm from the injector exit. Before this distance, there is not enough seeding particles and thus not enough valid vectors for statistics.

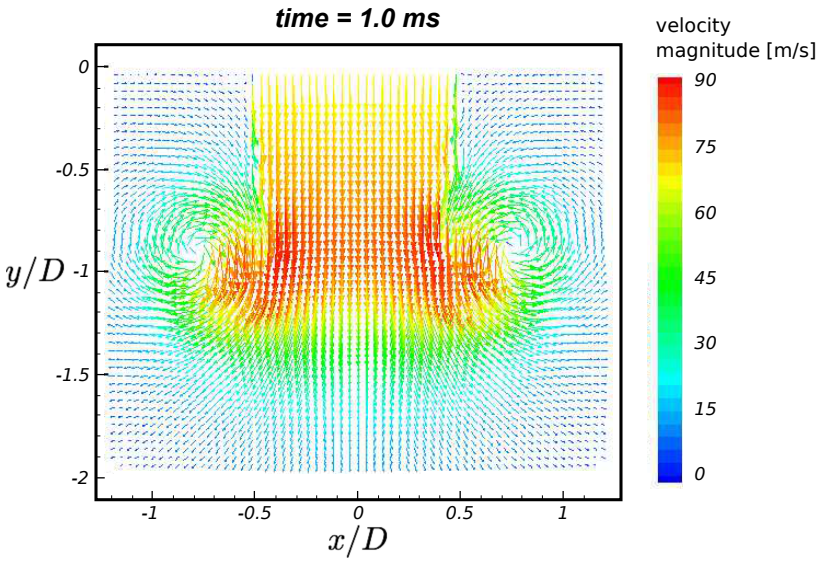

FIG. 6. Velocity field at the jet outlet, 1.0 ms after the injector opening.

An estimation of the measurement uncertainty was performed following the method proposed by Hesselink[36]. Half of the pixel size was used to estimate the uncertainty, so that $\text{Error}_{PIV} = \frac{1}{2}\frac{\Delta p}{\Delta t}$, with Δp the pixel size, and $\Delta t = 2\ \mu s$ is the delay between two laser pulses. This leads to a maximum error of 2.5 m/s, which will be used in the forthcoming sections to display error bars on the experimental results. Note that this value seems rather high compared to the maximum value of the cross-flow velocity (around 12 m/s). However, it represents less than 3% of the maximum jet velocity vector. Moreover, as mentioned by Westerweel[37], one should keep in mind that this is a pessimistic estimation that only reflects the largest possible error.

The PIV planes are shown in Fig. 7. One can also see the coordinate system used in this study: the origin is situated at the centre of the convergent-volume exit, x is the cross-flow streamwise direction, y the jet direction, and z the spanwise direction. Eight PIV planes were measured: four in the streamwise direction at locations $x = -1D$ (P1), $x = 0D$ (P2), $x = 1D$ (P3), $x = 2D$ (P4); and four in the spanwise direction at locations $z = 0D$ (P5), $z = 0.7D$ (P6), $z = 1.5D$ (P7) and $z = 5D$ (P8). The time reference in the study is the jet-opening time ($t = 0.0\ ms$). Hence, the following times were investigated $t = [0.6, 0.8, 1.0, 1.2, 1.4, 1.6, 1.8, 2.0, 3.0, 4.0, 5.0, 6.0, 7.0]\ ms$. Only the most relevant

planes/times will be presented in this paper.

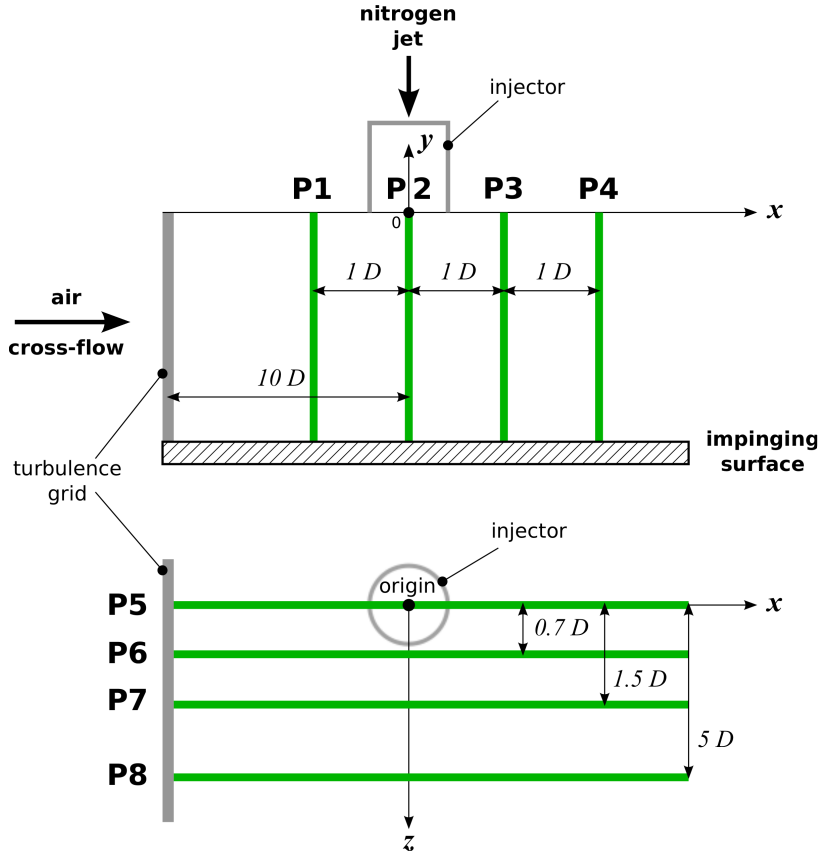

FIG. 7. Location of the PIV planes.

III. SET-UP OF THE NUMERICAL SIMULATIONS

A. Solver and subgrid-scale models

1. Numerical solver

The numerical solver used in this study is AVBP [http://www.cerfacs.fr/4-25719-Publications.php]. It is a parallel code that offers the possibility of handling structured or unstructured grids in order to solve the full 3D compressible reacting Navier-Stokes equations with a cell-vertex formulation. The efficiency and accuracy of the solver have been widely presented and demonstrated in academic and industrial configurations in the past years (see Ref.[38–40], among many others). The resolved equations are the Favre-filtered compressible equations

for the conservation of mass, momentum, species mass fractions, and energy. The numerical method used is described later in section IV A 1.

Concerning the subgrid-scale model, a functional approach is used in AVBP for the SGS kinematic viscosity, ν_{SGS}, defined as:

$$\nu_{\mathrm{SGS}} = (C\Delta)^2\mathcal{D}, \tag{1}$$

where Δ is the filter length (the cube root of the cell volume), $\mathcal{D}$ the time-scale operator and C the model constant. When C does not vary in space and time the model will be referred to as a "static" model. Contrarily, when C varies in space and/or in time, it will be referred to as a "dynamic" model. Two SGS models are tested in this study: the static σ-model[2] and the dynamic Smagorinsky model[1] implemented under its simplest form (local averaging and clipping of negative values). These two models were selected because they share common properties, while differing in essence as explained in the following sections. A more advanced formulation of the dynamic Smagorinsky model could have been tested, for instance the one proposed by Meneveau *et al.*[9], but it was preferred to limit the current study to the standard dynamic Smagorinsky model as it is the one mainly used for LES of complex industrial configurations. However, since the present experimental database is available upon request, any collaborator is strongly encouraged to test their SGS-model of preference.

Note that in this paper the large-scale filtered quantities do not have a specific notation. For instance, the filtered velocity components in the x, y and z directions will be noted u, v, and w, respectively.

2. The σ-model

This model has been recently developed by Nicoud *e*t al.[2]. The static version of the model was used in this study and the model constant, C_σ, was set here to 1.5. The time-scale operator, $\mathcal{D}_\sigma$, is defined as:

$$\mathcal{D}_\sigma = \frac{\sigma_3(\sigma_1-\sigma_2)(\sigma_2-\sigma_3)}{\sigma_1^2}, \tag{2}$$

where $\sigma_1 \leq \sigma_2 \leq \sigma_3$ are the singular values of the velocity gradient tensor, $\frac{\partial u_i}{\partial x_j}$. This formulation has several interesting properties compared to other static models. Indeed, it is

able to vanish for a various number of canonical laminar flows, for which no SGS viscosity is expected: two-dimensional or two-component flows, axisymetric and isotropic compression/dilatation. Furthermore, it also has the proper cubic behaviour in near wall regions and thus does not require any local dynamic procedure. The model was validated against different academic cases (homogeneous isotropic turbulence, turbulent channel, periodic free jet), and with different numerical solvers[2,41].

3. The dynamic Smagorinsky model

This model was developed by Germano *et* al.[1] in order to improve the performances of the Smagorinsky model[3]. In this model, the time-scale is expressed as follows:

$$\mathcal{D}_s = \sqrt{2S_{ij}S_{ij}}, \tag{3}$$

where S_{ij} is the velocity strain rate based on the filtered velocity field u_i. The Smagorinsky time scale strongly increases in shear flows and also in some canonical laminar flows. In order to compensate these drawbacks the constant is calculated dynamically using the Germano-identity[1]. Following the proposition of Lilly[42], the model constant from the dynamic procedure is computed using a least squares approach:

$$(C_s\Delta)^2 = -\frac{L_{ij}M_{ij}}{2M_{ij}M_{ij}}, \tag{4}$$

where $L_{ij} = \widehat{u_iu_j} - \hat{u}_i\hat{u}_j$ is the (modified) Leonard term based on the grid-based filter and the test filter $\hat{\cdot}$, and M_{ij} is directly related to the differential operator of the underlying eddy-viscosity model and reads:

$$M_{ij} = \frac{\hat{\Delta}^2}{\Delta^2}\widehat{\mathcal{D}_s}\widehat{S_{ij}} - \widehat{\mathcal{D}_sS_{ij}}, \tag{5}$$

where $\hat{\Delta}$ stands for the test-filter characteristic-length. Unfortunately, the original dynamic procedure most often requires some averaging in order to reduce the constant variability over space and time. Several improved versions of the dynamic Smagorinsky model were proposed to handle configurations where no homogenous directions are present[8,9], which potentially stabilises the model for complex configurations. Still, a common practice with complex geometries is to apply the least square formula over a small volume surrounding

the grid-point of interest, and to clip the remaining negative values of the dynamic constant. This means that Eq. 4 is replaced by the following equation:

$$(C_s\Delta)^2 = max\left[-\frac{< L_{ij}M_{ij} >_{loc}}{2 < M_{ij}M_{ij} >_{loc}}, 0\right], \tag{6}$$

where $< \cdot >_{loc}$ stands for a volume integral evaluated on a small local-volume (typically the surrounding cells).

B. Geometry simplification and space discretization

The whole experimental apparatus was not simulated in order to save computational time. However, the computational domain was defined so that the boundary conditions are located where the geometry and the flow conditions are well known. This is a necessary condition in order to reproduce the experimental flow with a good level of fidelity. For instance, the whole jet-injection system was not included in the computational domain because the internal geometry of the injector was unknown. This issue was overcome by starting the computational domain at the jet convergent-volume. Moreover, the cross-flow convergent volume, the honeycomb, and the turbulence grid were not included in the domain to save some computational time, notably because the space discretization of the turbulence-grid holes would have considerably reduced the time-step of the numerical solver. Finally, the whole exhaust pipe was truncated because the real dimensions are too large to be taken into account. However, the pipe length was kept long enough to ensure that the boundary condition is located in a region where the flow is relatively well developed, and where the large-scale recirculating structures appearing in the chicane do not influence the flow anymore. All these choices led to the simulation domain presented in Fig. 8. Note that the spanwise dimension of the working section was sufficiently small to be able to include the lateral walls as boundary conditions.

The space discretization plays an important role in the result quality, especially in large-eddy simulation, for which the cell-volume is directly related to the filter cutoff. To this regard, the computational domain was discretized with 12.7 million tetrahedral cells, which corresponds to 2.3 million nodes. As shown in Fig. 9, a particular attention was paid to the mesh resolution near the wall and in the jet convergent-volume. The mesh density was uniform around the injector diameter, in the streamwise direction for $-2.5D \leq x \leq 4.5D$

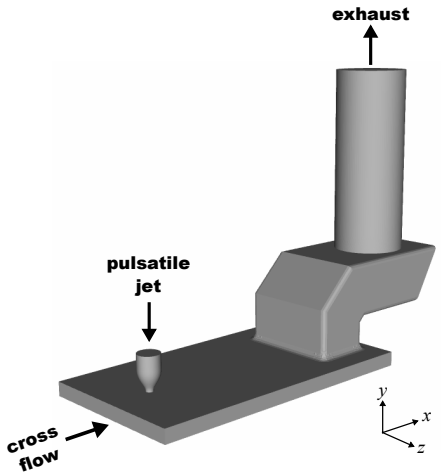

FIG. 8. Computational domain.

and in the spanwise direction for $-2D \leq z \leq 2D$. In the rest of the geometry, the mesh was progressively coarsened as shown in Fig. 9(b). In the region of interest, the size of the cells was chosen in order to have a mesh resolution of $4 \leq \Delta h^+ \leq 6$ in the vicinity of the wall, where $\Delta h^+ = \frac{\Delta h\, u_\tau}{\nu_w}$ is the normalised grid spacing, with ν_w the wall kinematic viscosity at the impinging surface temperature, and u_τ the wall friction velocity assessed with Dean's correlation[43] before the impingement of the jet, *i.e.* when only the cross flow is present (the mean centreline velocity was taken to 12 m/s). As shown in Fig. 9(a), this grid spacing was sufficient to have at least 30 nodes in the nozzle diameter in order to reproduce well the jet-velocity profile[44].

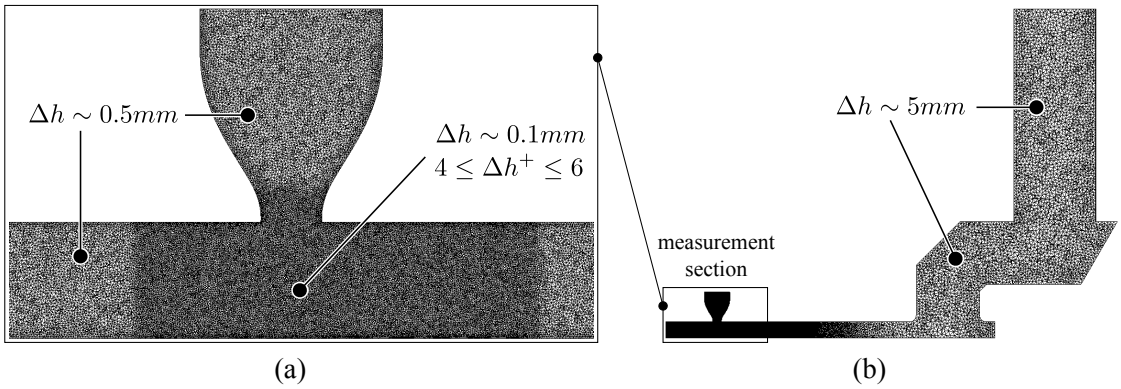

FIG. 9. Mesh refinement: (a) measurement section (b) whole computational domain.

C. Simulation strategy

The experimental results were converged using an ensemble average over 400 individual realizations. Each jet pulsation was separated by 1000 ms, and the jet remained opened during 10 ms. Reproducing exactly the same condition with the numerical simulation was not possible with the computational resources available. For this reason, a strategy similar to the one proposed by Cabrit & Nicoud[45] was used, which consisted of performing an ensemble average over different simulations whose initial solutions were different. In this way, each numerical simulation could be limited to a simulation-time of 10 ms, without simulating the 1000 ms between each pulsation.

To generate the different uncorrelated initial solutions, a first simulation was performed with the jet closed and the cross-flow boundary condition described in section III D 3. As illustrated in Fig. 10, the first part of this simulation was a transient phase, during which the turbulent state of the flow was converging towards a steady state. This transient phase lasted approximately 50 ms, which corresponded to a non-dimensional time-length of $17H/u_\tau$, with u_τ deduced from Dean's correlation[43] and a channel centreline velocity of 12 m/s. Once the steady state was reached, the simulation kept running and 10 independent instantaneous solution files were saved, each of them separated by 10 ms (approximately $3.5H/u_\tau$ in non-dimensional units). Then, these 10 uncorrelated instantaneous solutions were used as initial solutions for 10 large-eddy simulations performed with the pulsatile jet. As summarized in Fig. 10, an ensemble phase-average was performed over the 10 LES to obtain converged statistics. This number of simulations seems to be small compared to the 400 used for the experimental results. However, comparisons were performed between a single simulation and an ensemble-average over 10 simulations, and no major differences were observed at the early stages and notably during the vortex-ring formation and propagation. The comparison is not shown explicitly in the paper, but one can have an idea of this comparison looking at the results shown in section IV A 1 (analysis performed with a single simulation) and section IV A 2 (analysis performed with an ensemble-average over 10 simulations). For this reason, and because the computational resources were limited, it was decided to restrict the averaging procedure to a sample of 10 simulations. This was proved to be sufficient to converge the first-order statistics and to ensure that the vortex-ring dynamics could be analysed without introducing artefacts of statistical nature. However, it is acknowledged

that more than 10 simulations should be used if one wants to scrutinise the jet deflection at later stages (time $\leq 6\ ms$), which is not the aim in the present study.

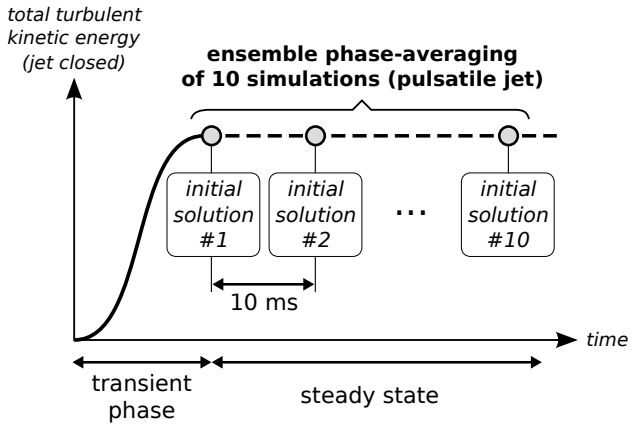

FIG. 10. Schematic of the ensemble-averaging strategy used to obtain a converged statistical representation of the flow.

D. Boundary conditions

Since a numerical solver for compressible flow was used, Navier-Stokes Characteristic Boundary Conditions (NSCBC)[46,47] were used at all the inlets, and three Dimensional Non-Reflecting Boundary Conditions (3D-NRBC)[48–50] at the outlet. No-slip boundary conditions were imposed at all walls in the working section (including the surface of the jet-impact), and law-of-the-wall boundary conditions[51] in the exhaust section where the mesh is coarser. The cross-flow and the jet-inlet boundary conditions are fully detailed hereafter.

1. Controlling the acoustic properties of the injector

Preliminary PIV measurements were performed without the cross-flow and without the impinging surface in order to properly characterize the jet-flow. These measurements gave access to the velocity profiles at the jet outlet, which were then integrated to estimate the time-evolution of the jet flow-rate (the velocity profile was assumed to be axisymetric, which was supported by the measurements). As depicted in Fig. 11, two phases can be distinguished: a strong unsteady phase (from 0 to 2.8 ms), and a quasi-steady phase (from 3.0 ms to 10 ms).

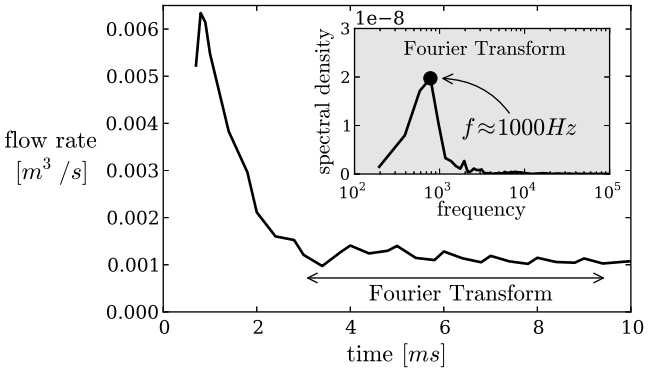

FIG. 11. PIV measurement of the jet flow-rate without the cross-flow, and without the impinging surface. The inner plot shows the premultiplied energy spectrum of the flow-rate computed for $t \geq 3.0\ ms$.

If one looks carefully at the quasi-steady phase, it can be seen that the flow-rate oscillates. As shown in Fig. 11, the first harmonic of the oscillations corresponds to a frequency of the injection system around 1000 Hz. This is due to the internal geometry of the jet convergent-volume (see Fig. 3), which varies sharply and acts as a Helmholtz resonator[52]. As shown in Fig. 12, such a resonator can be modelled as a succession of two ducts whose sections change rapidly, and whose fundamental acoustic frequency can be computed as:

$$f_H = \frac{c_0}{2\pi}\sqrt{\frac{S_2}{L_2 V_1}}, \tag{7}$$

where c_0 is the speed of sound, V_1 the volume of the first duct, L_2 the length of the second duct, and S_2 the section of the second duct.

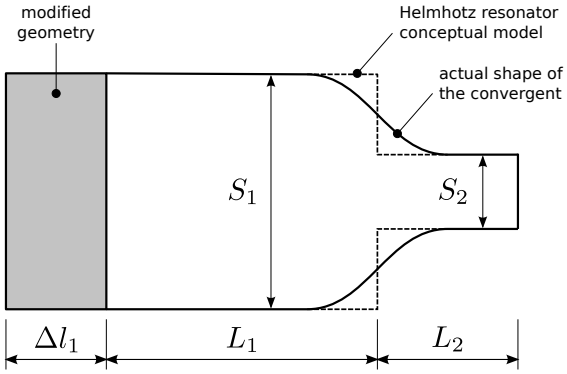

FIG. 12. Schematic of an Helmholtz resonator as described in Ref.[52].

A specific test case was designed in order to verify the acoustic response of the injec-

tor in the numerical simulation. To do so, a continuous flow-rate ($1.5 \times 10^{-3} m^3/s$) was imposed in the jet convergent-volume, and the frequency of the flow-rate was measured at the convergent-volume exit. As shown in Fig. 13 (top), the resulting frequency was about 1200 Hz, which differs from the expected 1000 Hz observed in the experiment. This is a well-identified problem in such compressible flow simulations, for which it is recommended to take into account the whole injection system[27]. However, as explained above, the injector geometry was unknown and could not be included in the simulation. To recover the expected natural frequency, $f_{\text{target}} = 1000\ Hz$, it was decided to control the acoustic properties of the convergent-volume by modifying its geometry. According to Eq. 7, this can be done by modifying the volume of the first duct, V_1. If the section of the first duct is unchanged, the change of duct length, Δl_1, can then be computed as follows:

$$\Delta l_1 = \frac{c_0^2}{4\pi^2} \frac{S_2}{S_1 L_2} \left(\frac{1}{f_{\text{target}}^2} - \frac{1}{f_{\text{real-shape}}^2} \right), \tag{8}$$

where $f_{\text{real-shape}} = 1200\ Hz$ is the frequency obtained in the simulation when the convergent volume has exactly the same dimensions as in the experiment. Hence, the geometry of the convergent volume was modified by $\Delta l_1 = 13.2\ mm$, which reproduces the expected acoustic behaviour of the injector as shown in Fig. 13 (bottom).

2. Imposing the jet flow-rate

The best method found to reproduce the experimental velocity profile at the injector exit consisted of imposing a non-reflecting condition at the convergent-volume inlet and a source term, $\mathcal{S}_y$, in the vertical (y-direction) momentum conservation equation. This source term was imposed only in a small volume Ω of the injector (between the planes $y = 10\ mm$ and $y = 20\ mm$ as shown in Fig. 13) and its formulation was as follows: $\mathcal{S}_y = \frac{1}{\tau}(Q_y - Q_{y,\text{target}})$, where $Q_y = \frac{1}{\Omega} \int_\Omega \rho v d\Omega$ and τ was a relaxation coefficient set to $9 \times 10^{-7}\ s$ during the entire simulation. In practice, $Q_{y,\text{target}}$ was determined thanks to the integration of the velocity profile measured at a location close to the injector exit, $y = -1.5\ mm$, in the pulsatile impinging jet in cross-flow configuration, and assuming that the density ρ was constant. As depicted in Figs. 14 and 15, the flow-rate was properly imposed thanks to this procedure, and the expected velocity profiles were recovered very close to the injector exit. Note, however, the presence of the overshoots on the velocity profiles at the early stages of the numerical

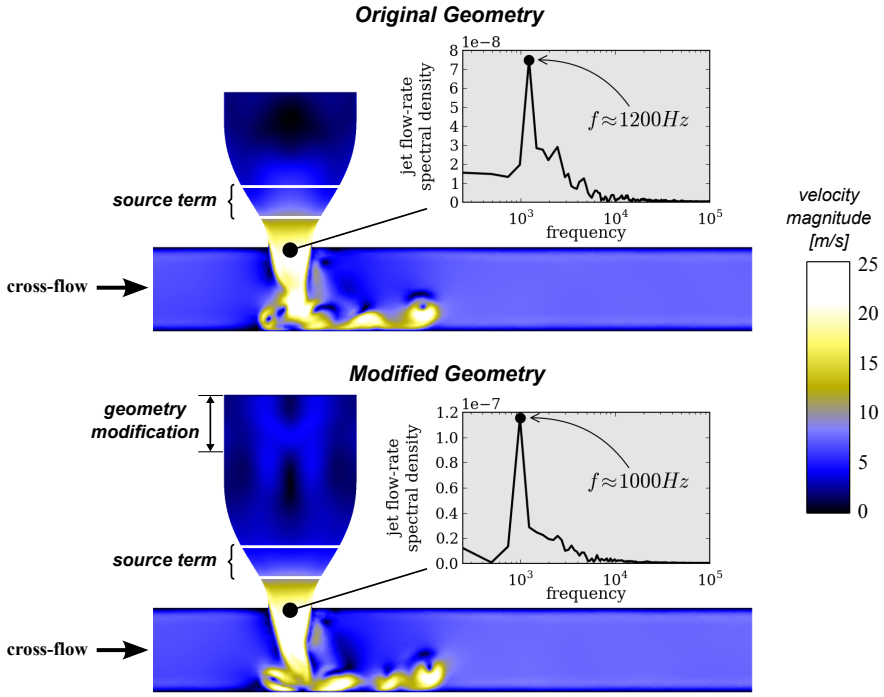

FIG. 13. Test case designed to verify the acoustic properties of the injector, and measurement of the jet flow-rate frequency at the injector lip: (top) original geometry, (bottom) modified geometry. The flow-rate is fixed to $1.5 \times 10^{-3} m^3/s$ in both cases.

simulation (time $\leq$ 1.0 ms). This is a common flow feature observed during the vortex rings formation (rolling-up phase and circulation production) at nozzle exit at early timings (see Fig. 8 in[28]). It is caused by the acceleration of the mass flow rate at the beginning of the injection. It is possible that these overshoots do not appear in the experimental results because they have been filtered out by the averaging procedure over 400 snapshots, and because the resolution of the LES is finer than the one in the PIV measurements (see section II C). Note that these overshoots were observed in each LES independently of the numerical scheme and the SGS-model used.

3. Imposing the turbulent cross-flow

One of the challenges for the numerical simulation was to properly account for the turbulent cross-flow without simulating the whole system. Indeed, taking into account the honeycomb, the convergent volume, and the turbulence grid down to the discretisation of the grid holes would have considerably increased the number of points while drastically de-

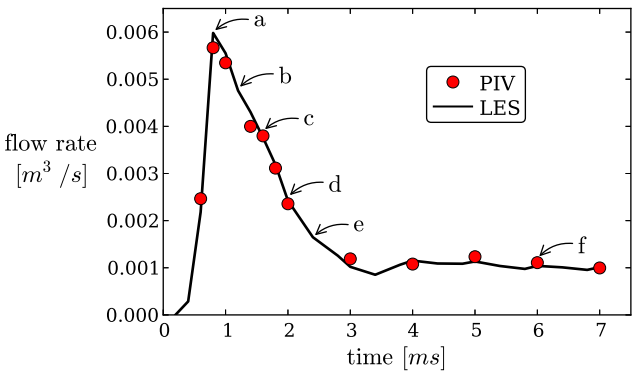

FIG. 14. Flow-rate measured at the jet convergent-volume outlet in the experiment and in the LES performed with the dynamic Smagorinsky model averaged over 10 realizations (similar results were obtained with the σ-model). The letters a-f refer to the subfigures of Fig. 18.

creasing the solver time-step (see section III D). Instead, the PIV measurements were used in order to extract the turbulent cross-flow statistics generated by the turbulence grid, and to impose these properties at the inlet boundary condition.

Figure 16 presents the mean streamwise velocity profiles extracted from the planes P5 ($z = 0D$), P6 ($z = 0.7D$), P7 ($z = 1.5D$) and P8 ($z = 5D$), at $x = -4D$. One can first note that the streamwise mean velocity is higher at the top wall than at the bottom one. This is due to the heterogeneous turbulence grid (see section II B) used in order to reduce the impact of the cross-flow on the vortex-ring propagation along the wall, while sufficiently deviating the jet. Moreover, although the grid was homogeneous in the spanwise direction, some discrepancies were observed among the different spanwise locations. Note, however, that the spanwise differences stay below the measurement uncertainty of the PIV (approximately 2.5 m/s, as already discussed in section II C). Hence, the averaged profile shown in Fig. 16 was uniformly imposed across the whole boundary condition. The two other mean velocity components were set to zero as suggested by the measurements. Concerning the turbulence statistics, the PIV measurements at $x = -4D$ were used to extract the different components of the Reynolds-stress tensor, namely $\overline{u'^2}$, $\overline{v'^2}$ and $\overline{u'v'}$ (the operator $\overline{\cdot}$ stands for the ensemble average performed over the available PIV data). The other components ($\overline{w'^2}$, $\overline{u'w'}$, $\overline{v'w'}$) were considered negligible. It is important to note at this stage that because of the limitation imposed by the narrow optical access in the experiment, the cross-flow statistics could only be extracted at a distance $x = -4D$. However, the simulated

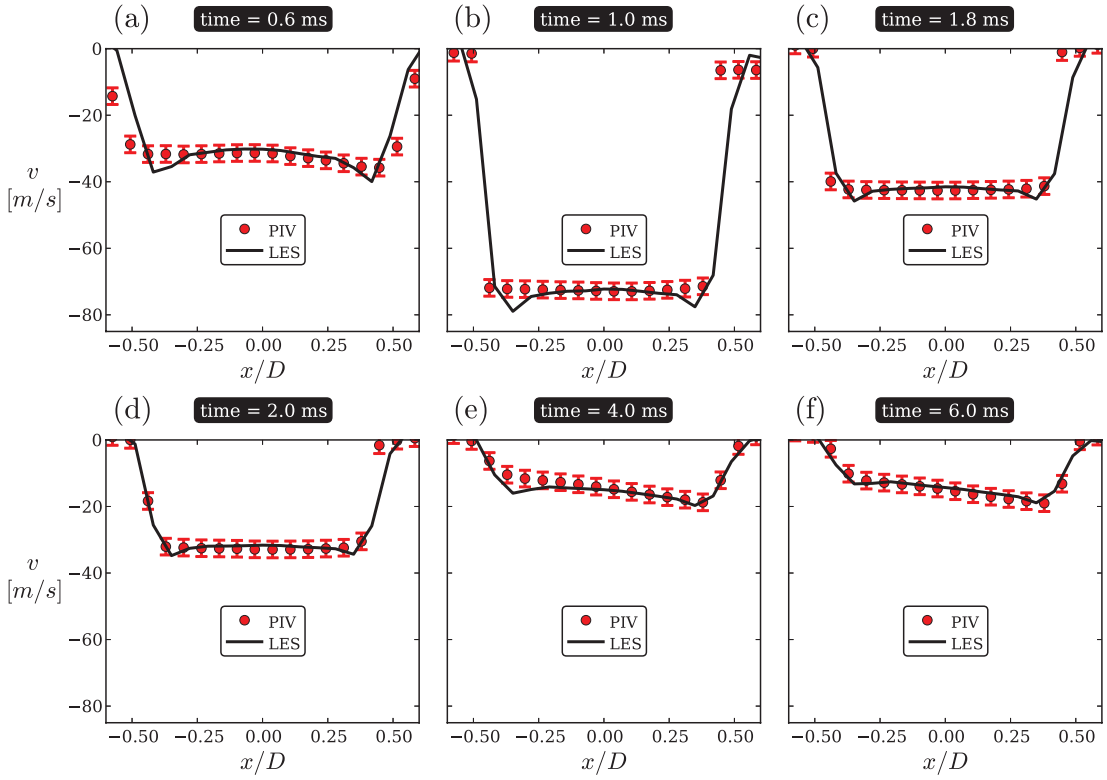

FIG. 15. Jet velocity profile in plane P5 close to the jet convergent-volume exit ($y = -1.5\ mm$). Simulation averaged over 10 realizations, and performed with the dynamic Smagorinsky model and the Lax-Wendroff numerical scheme.

domain started at $x = -10D$, and the flow development was assumed to be negligible between $x = -10D$ and $x = -4D$. This deportation of the boundary condition was justified by the measurement of the cross-flow velocity at different streamwise locations.

In order to impose these mean and turbulent quantities in the numerical simulation, the procedure proposed by Guezennec and Poinsot[53] was used for injecting turbulence via non-reflecting characteristic boundary conditions. This technique was coupled with the Random Flow Generation (RFG) procedure of Smirnov *et al.*[54]. This procedure is based on a superposition of harmonic functions, which leads to the generation of time varying velocity fields respecting two constraints. First, the energy spectrum matches a predefined function (here, $E(k) = 16\left(\frac{2}{\pi}\right)^{1/2} k^4 exp(-2k^2)$ as proposed in the original paper of Smirnov *et al.*[54]). Second, the Reynolds-stress tensor components respect a target value, set here to the ones measured with the PIV measurements as described in the previous paragraph. To complete the RFG procedure, the turbulence length-scale was set to $H/3$, and the integral to turbulent

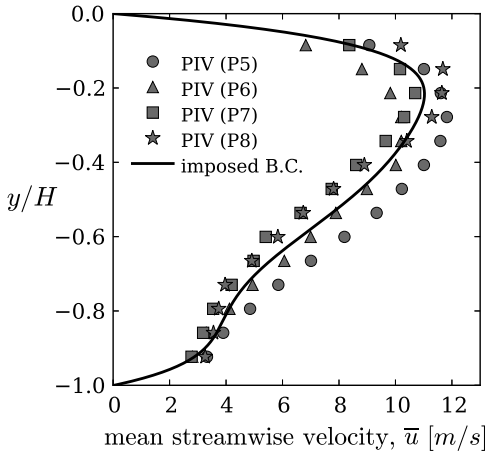

FIG. 16. Mean streamwise cross-flow velocity profiles at $x = -4D$ for the available PIV planes. The imposed boundary condition is an average of the available profiles.

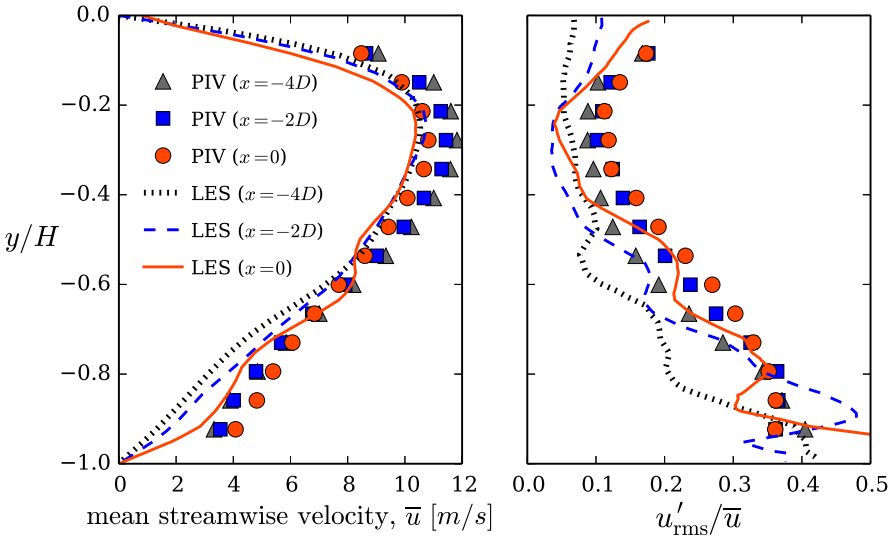

FIG. 17. Streamwise development of the cross-flow in the PIV measurements and the LES performed with the dynamic Smagorinsky model (similar results were obtained with the σ-model): (left) mean streamwise velocity, (right) normalised streamwise turbulence intensity. The profiles are extracted from plane P5 ($z = 0$), at $x = -4D$, $x = -2D$, and $x = 0$.

length-scale ratio was set to 2, as advocated for this type of channel flow configuration.

A comparison of the cross-flow obtained with the LES and the PIV measurements is proposed in Fig. 17, for the region of interest ($-4D \leq x \leq 0$). The mean streamwise component and the normalised streamwise turbulence intensity profiles obtained with the

LES agree well with the PIV measurements, the differences observed staying in the maximum measurement uncertainty. This comparison illustrates the efficiency of the procedure used to impose the cross-flow boundary condition.

IV. EXPERIMENTAL AND NUMERICAL RESULTS

A. Comparison of the velocity fields

A sequence showing the flow topology after the jet opening is presented in Fig. 18. A vortex-ring is first generated at the injector mouth (Fig. 18(a)) and propagates downwards (Fig. 18(b)). Then, this coherent vortex-ring impacts the wall surface and smaller structures appear (Fig. 18(c) and Fig. 18(d)). At later instants, the jet flow-rate decreases and the jet is deflected by the cross-flow (Fig. 18(e) and Fig. 18(f)). Overall, two main phases are observed: during the first one the vortex-ring impacts the plate; during the second one the jet is deflected. This is summarised in Table I, which also gives the characteristic density and momentum-flux ratios during these two phases.

phase	density ratio $\left(\frac{\rho_{\text{jet}}}{\rho_{\text{cf}}}\right)$	momentum-flux ratio $\left(\frac{\rho_{\text{jet}}U_{\text{jet}}^2}{\rho_{\text{cf}}U_{\text{cf}}^2}\right)$	time
vortex-ring formation	0.83	45	time $\leq 2.5\ ms$
jet deviation	0.83	1.5	time $\geq 2.5\ ms$

TABLE I. Characteristic density ratio and momentum-flux ratio during the two main phases of the flow. ρ_{jet} and ρ_{cf} are the fluid density in the jet and the cross-flow, respectively. U_{jet} is the maximum jet velocity and U_{cf} the maximum cross-flow velocity.

Due to the important range of scales generated in this flow, it was anticipated that the numerical results could be sensitive to both the numerical scheme and the SGS model. This is investigated hereafter in two different sections.

1. Influence of the numerical scheme

Large-eddy simulations of academic test-cases are often performed with non dissipative spectral methods, which generally cannot be used for industrial applications (these high-order schemes require periodic boundary conditions and simple computational domains).

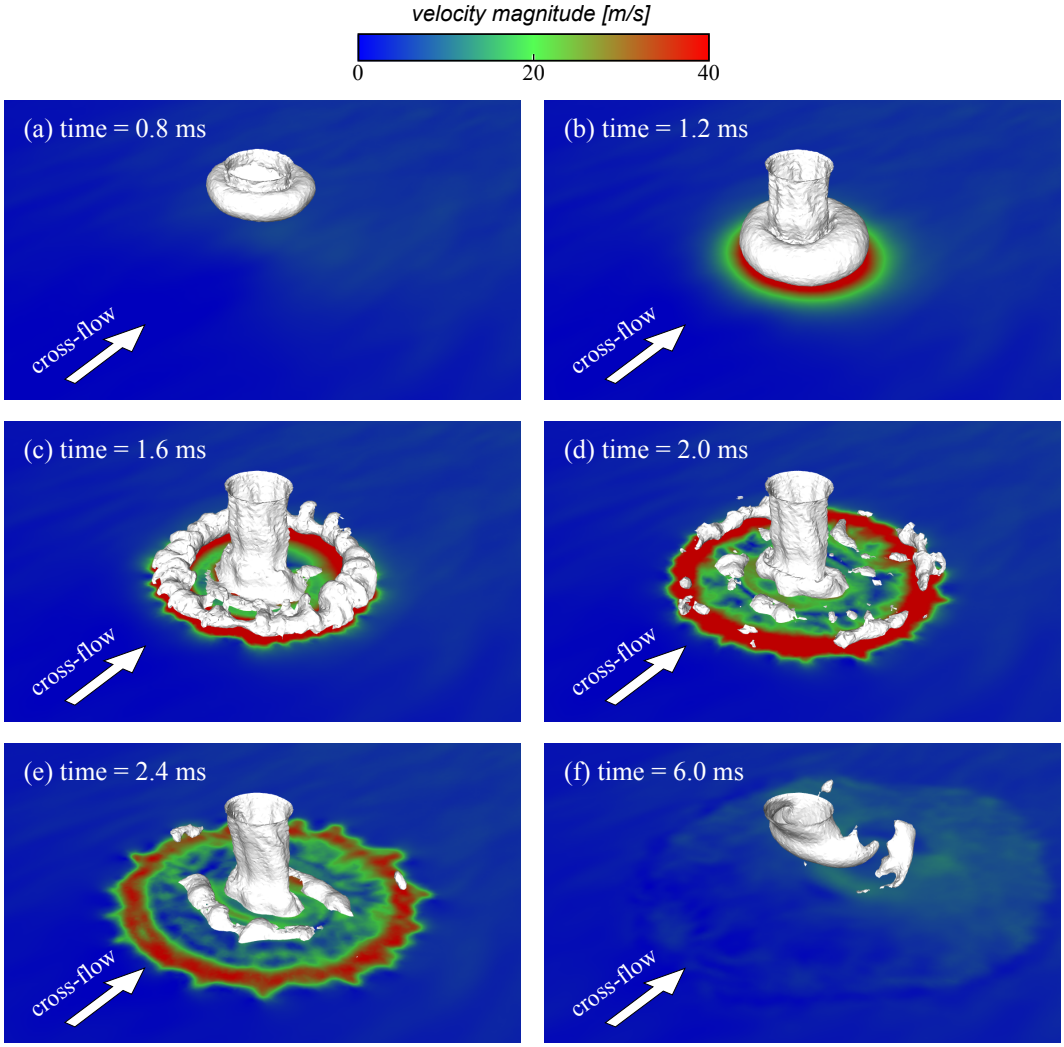

FIG. 18. Sequence showing the impact of the vortex-ring generated by the pulsatile jet. White iso-surface: temperature ($T = 325K$) delimiting the hot flow coming from the jet and the cold cross-flow. Colored plane: velocity magnitude 1.5 mm above the flat plate. The corresponding jet flow rates for the different times are shown in Fig. 14.

Since the configuration of interest here can be more suitably simulated with a finite-volume or a finite-element approach, the sensitivity of the LES to the numerical scheme was investigated. Two different schemes were tested, while using the same SGS model (the dynamic Smagorinsky model). The first one, GRK, is the usual finite-element Galerkin numerical scheme[38,55], 4^{th}-order centered in space, with a 3^{rd}-order Runge-Kutta temporal integration. The second one is the Lax-Wendroff (LW) numerical scheme[56,57], which is a centered finite-volume numerical scheme 2^{nd}-order accurate in both space and time. It is obtained by

performing a time centered second-order Taylor development and by replacing the temporal derivatives with spatial derivatives, introducing the flux Jacobian. This second order term is a stabilizing term but it is also responsible for the dissipation of small scales of turbulence contrary to the three-step Runge-Kutta finite volume scheme GRK. Details on the LW scheme as implemented into AVBP may be found in[39]. These two schemes are considered "LES compatible" since their dissipation at small wavelengths is sufficiently low to not interact with the dissipation of the SGS-model. The main difference between the two schemes resides in their dispersion properties, LW being more dispersive than GRK (see Fig. 14 in Ref.[38]). However, the Lax-Wendroff scheme is more often used in LES of industrial configurations because it is 2.5 times less CPU demanding than the GRK scheme, and because its stabilisation term prevents the emergence of wiggles. The properties of the two numerical schemes are summarized in table II. Both schemes are implemented into AVBP within a cell-vertex formulation[58].

scheme	space-accuracy	time-accuracy	CPU cost	method
GRK	4^{th}-order	3^{th}-order	2.5	finite elements
LW	2^{nd}-order	2^{nd}-order	1	finite volumes

TABLE II. Properties of the two numerical schemes used in this study. The CPU cost is normalised by the cost of a simulation performed with the Lax-Wendroff scheme (LW).

The two numerical schemes are compared in Fig. 19 against the PIV measurements. The initial solution was the same in both cases, and the results were not ensemble averaged. Both numerical schemes give qualitatively the same predictions. Before the impingement, the vortex-ring formation is well predicted. After the impact ($t \geq 1.6\ ms$), as shown in Fig. 19(d), the propagation of the vortex on the solid surface is clearly under-predicted in both cases. This demonstrates that this issue is most likely not due to the accuracy of the numerical scheme (this will be developed in the next section IV A 2). In the later stages, however, the deviation of the jet is well predicted. Overall, one can distinguish in Fig. 19 that the dynamics of the flow is governed by two distinct mechanisms: (1) during the early stages the jet momentum imposes its motion to the flow; (2) during the late stages the cross-flow momentum dominates the flow and deviates the jet.

A precise comparison between the two numerical schemes is given in Fig. 20, in which the

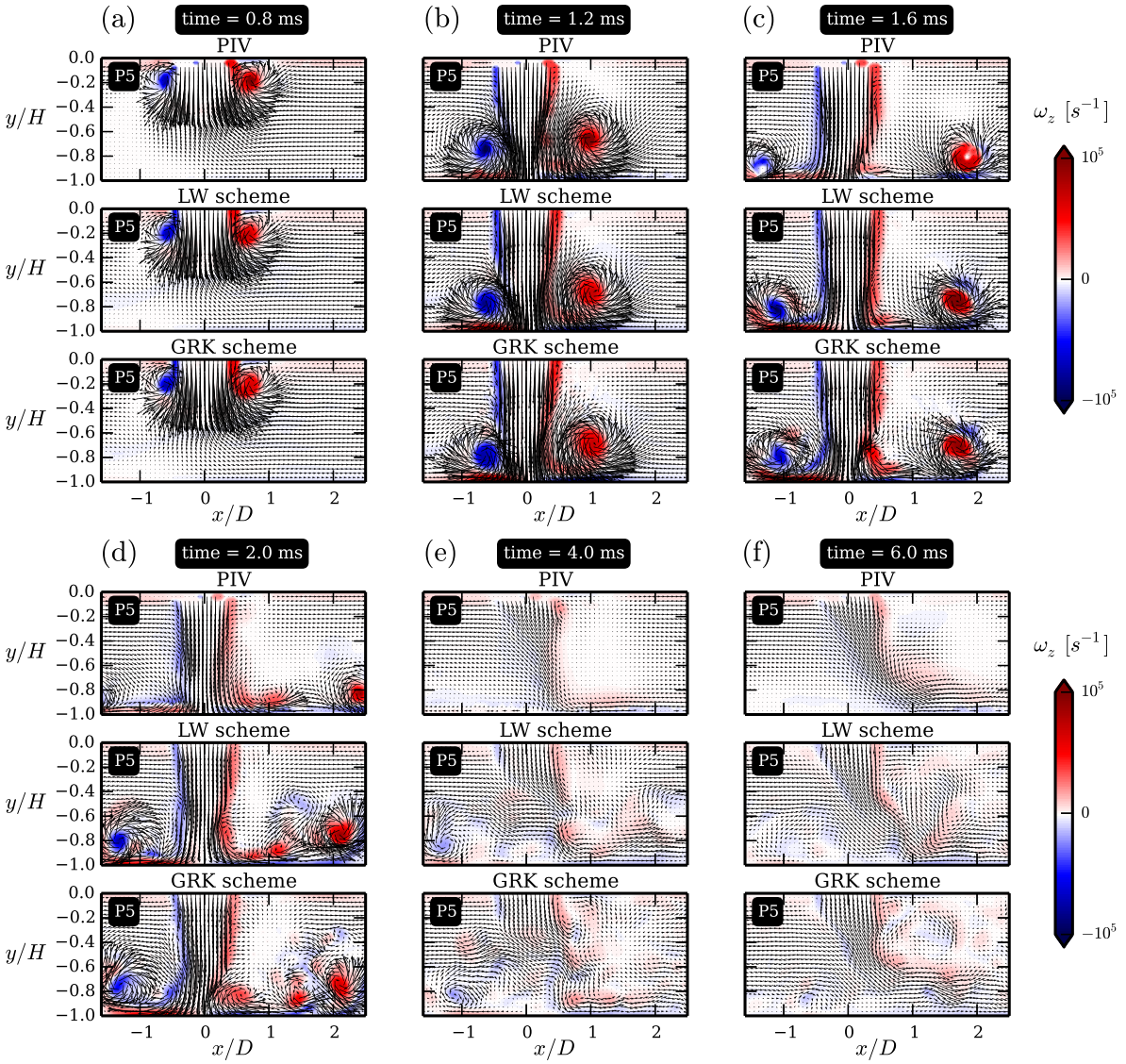

FIG. 19. Velocity vectors and vorticity (blue and red) field showing the influence of the numerical scheme in plane P5 ($z = 0D$). Both large-eddy simulations were performed with the dynamic Smagorinsky model and not ensemble-averaged (a single realization is shown).

velocity profiles are shown for two different locations ($y = -1D$ and $y = -1.5D$). The slight differences observed can be of statistical nature since a single realization was performed for each numerical scheme (no ensemble averaging). Note, however, that the circulation of the vortex-ring segments was computed, and no major differences were observed (not shown). The overall agreement between the two numerical schemes demonstrates that the numerical errors do not impact the present LES, at least with the two numerical schemes tested which are "LES compatible"[38,39,59]. This result is obviously not general and strongly depends on

the configuration of interest and the quality of the spatial discretisation. In the present case, this is an indicator of the good quality of the mesh resolution.

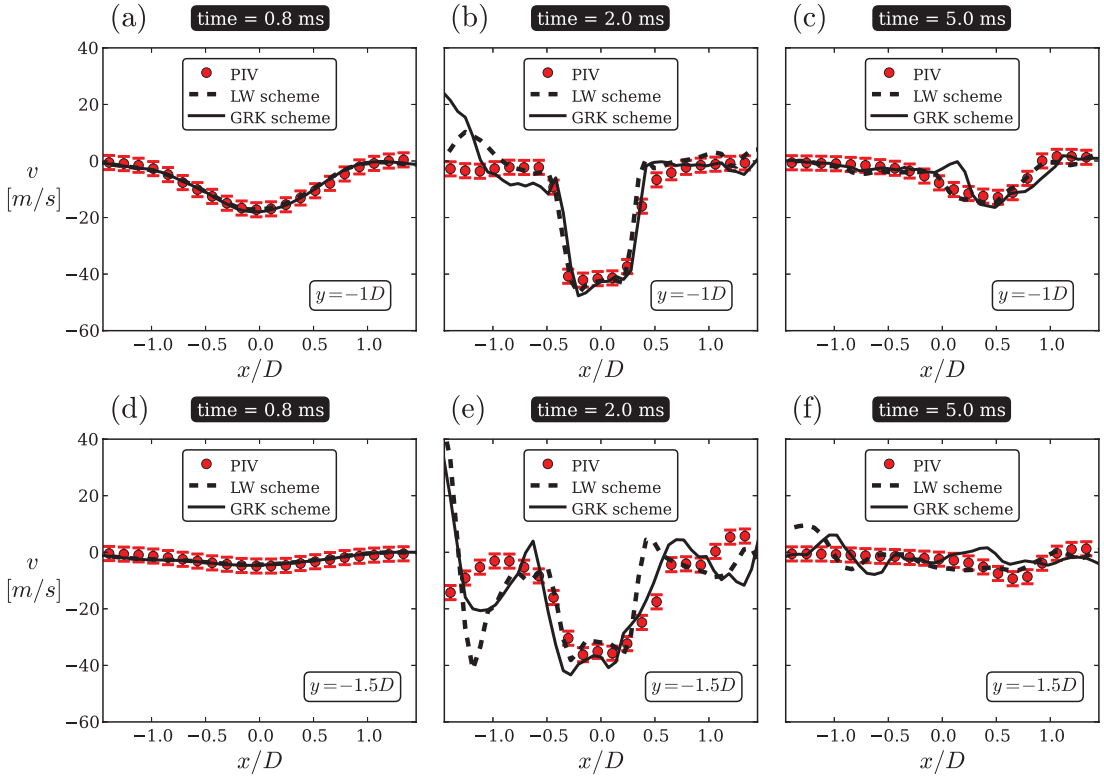

FIG. 20. Influence of the numerical scheme on the vertical velocity profile, v, in plane P5 ($z = 0D$), for two different locations: (a,b,c) $y = -1D$, (d,e,f) $y = -1.5D$. LES results are not ensemble-averaged and correspond to a single realization.

2. Influence of the SGS model

The influence of the SGS viscosity model was investigated by comparing the predictions obtained with the σ-model and the dynamic Smagorinsky model. The Lax-Wendroff scheme was used for both cases since it was shown in the previous section IV A 1 that this numerical scheme offers the same level of prediction as the Galerkin scheme (GRK), while being 2.5 times less CPU demanding. For an accurate comparison, the results gathered in Fig. 21 were ensemble-averaged over 10 independent simulations as explained in section III C.

The two SGS models give similar results for the early stages (Fig. 21(a) and Fig. 21(b)). As already illustrated in Fig. 19, this is not surprising since this phase is governed by well-

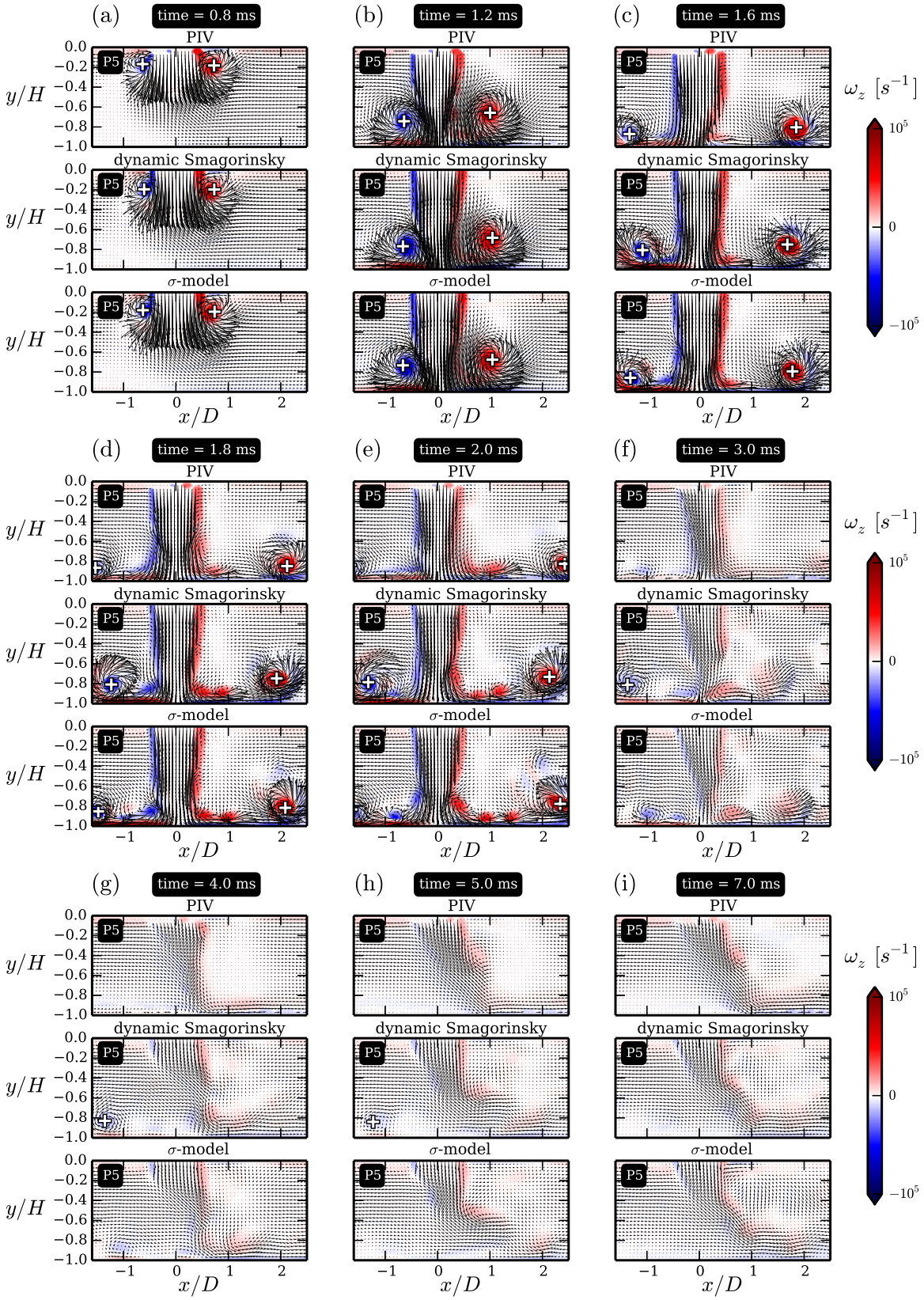

FIG. 21. Velocity vectors and vorticity (blue and red) field showing the influence of the SGS viscosity model in plane P5 ($z = 0D$). White crosses indicate the position of the vortex-ring cores. LES results averaged over 10 realizations.

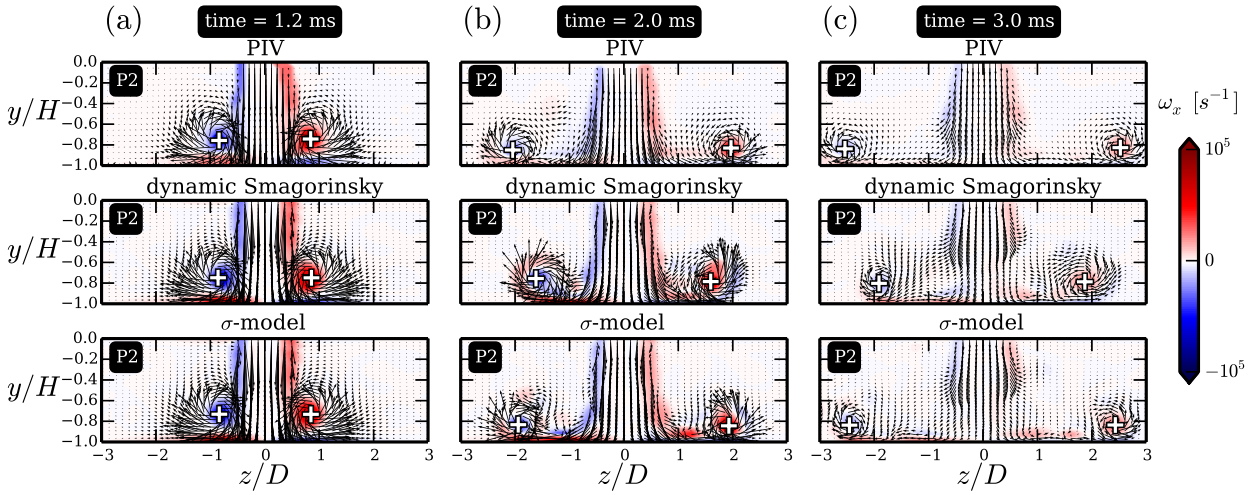

FIG. 22. Velocity vectors and vorticity (blue and red) field showing the influence of the SGS viscosity model in plane P2 ($x = 0D$) perpendicular to the cross-flow. White crosses indicate the position of the vortex-ring cores. LES results averaged over 10 realizations.

resolved, large-scale structures induced by the high jet flow-rate (see Tab. I). The differences between the two SGS-models are mainly visible in the second phase, when the vortex-ring interacts with the wall (Fig. 21(c) to Fig. 21(e)). Indeed, while the flow is well reproduced by the σ-model, it appears that the dynamic Smagorinsky model failed to predict the adequate convection velocity of the vortex-ring. This is especially visible upstream, in the region $x < 0$. For the dynamic Smagorinsky model, one can see in Fig. 21(e), Fig. 21(f), Fig. 21(g), and Fig. 21(h) that the vortex-ring stops its upstream motion at $x \approx -1.5D$. On the contrary, the vortex-ring is no longer visible at the same stages for the PIV measurements and the σ-model simulation because it managed to travel outside the visualisation window. For the later stages, the two SGS-models are able to properly reproduce the jet deflection.

Hence, the main differences are observed during the vortex-ring convection over the wall. This was confirmed by the analysis of all the other available planes, notably the planes perpendicular to the cross-flow, in which the vortex-ring propagation can be observed in the spanwise direction. For instance, the plane $x = 0D$ is presented in Fig. 22, where the convection velocity of the vortex-ring is clearly underestimated by the dynamic Smagorinsky model. On the contrary, the σ-model gives better results, even at later stages (Fig. 22(b) and Fig. 22(c)).

The velocity profiles in plane P5 ($z = 0$) at $y = -1D$ are presented in Fig. 23. The

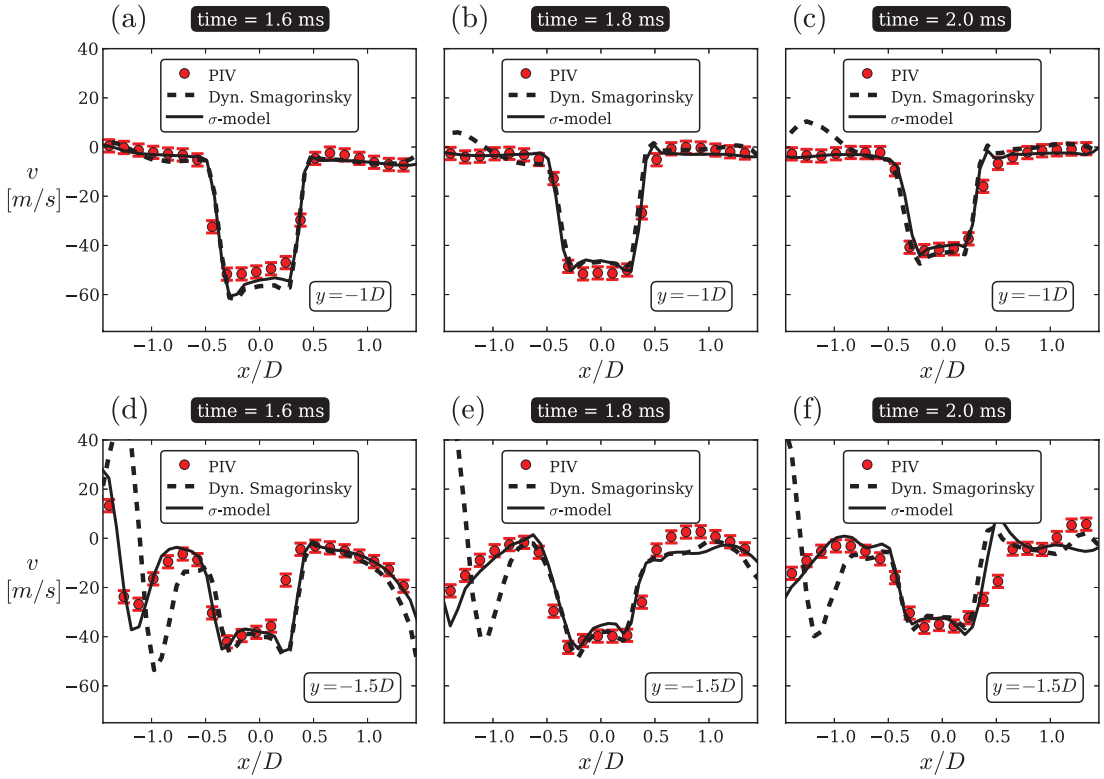

FIG. 23. Influence of the SGS viscosity model on the vertical velocity profile, v, in plane P5 ($z = 0D$), for two different locations: (a,b,c) $y = -1D$, (d,e,f) $y = -1.5D$. LES results averaged over 10 realizations.

predictions are similar at early stages (Fig. 23(a) to Fig. 23(c)), but only the σ-model is able to properly reproduce the expected velocity profiles at later stages. The large errors and the wrong peak location observed with the dynamic Smagorinsky model (Fig. 23(d) to Fig. 23(f)) are also good indicators of the underestimation of the upstream vortex-ring convection. However, during the later stages ($t > 2.5\ ms$), both models give very close predictions (not shown here).

V. DISCUSSION

In order to better quantify the differences between the two models, the vortex core trajectories were determined in the two planes P2 and P5 using a procedure similar to the one

proposed by Couch & Krueger[60]. P2 and P5 are chosen because they are, respectively, the planes where the cross-flow has the minimum and the maximum influence on the vortex-ring propagation. P2 can help quantifing the effect of the SGS viscosity only, and P5 the combined effect of the SGS viscosity and the cross-flow. First, a threshold of 20% of the maximum absolute vorticity was applied to the vorticity field. Next, the location of the vortex core was determined by computing the centroid of the retained vorticity contained in a square domain of side-length $0.5D$ centred on the maximum absolute vorticity location. The vortex core locations are represented by a white cross in Fig. 21 and Fig. 22. Finally, the circulation, Γ, associated with each vortex was found by applying Stokes's formula in a square of side-length $0.5D$ centred on the vortex core.

Figures 24 and 25 show the vortex core trajectories coloured by the absolute circulation in plane P5 ($z = 0$) and P2 ($x = 0$), respectively. It is important to note that in contrary to the case of an isolated vortex in which the circulation decays faster when dissipation increases, there is no straightforward correlation between the circulation and the dissipation rate of the vortex ring during the wall-vortex interaction. This was already observed in previous works (e.g.[61]). As shown in the Fig. 10 of this article, the circulation remains the same for different Reynolds number configurations although the propagation of the vortex dynamics during the impingement is not the same. A chronological analysis of the vortex-ring dynamics is proposed in the following paragraphs to describe the scenario responsible for the differences observed between the two SGS viscosity models tested in this paper.

Before the impact of the vortex-ring ($t \leq 1.2\ ms$, first four vortex core positions in Fig. 24 and Fig. 25), the trajectories of the vortex cores and the circulation are both well captured by the two large-eddy simulations. During this range of time, the vortex-ring propagates symmetrically around the jet axis in plane P2 (Fig. 25) since this plane is free of any cross-flow. Meanwhile, the vortex-ring segment situated in plane P5 (Fig. 24) is subjected to a cross-flow interaction, which deviates the vortex core trajectories and modify the circulation. Indeed, as reported by Lim *et al.*[62] and Cheng *et al.*[63], the presence of the cross-flow has two direct impacts on the vortex-ring propagation: (1) it convects the vortex-ring downstream (in the x-direction); (2) the background vorticity induced by the cross-flow modifies the circulation balance between each vortex segment, which tilts the vortex-ring depending on the sign of the background vorticity. Both SGS viscosity models give the same level of prediction during this phase ($t \leq 1.2\ ms$), and are notably able to

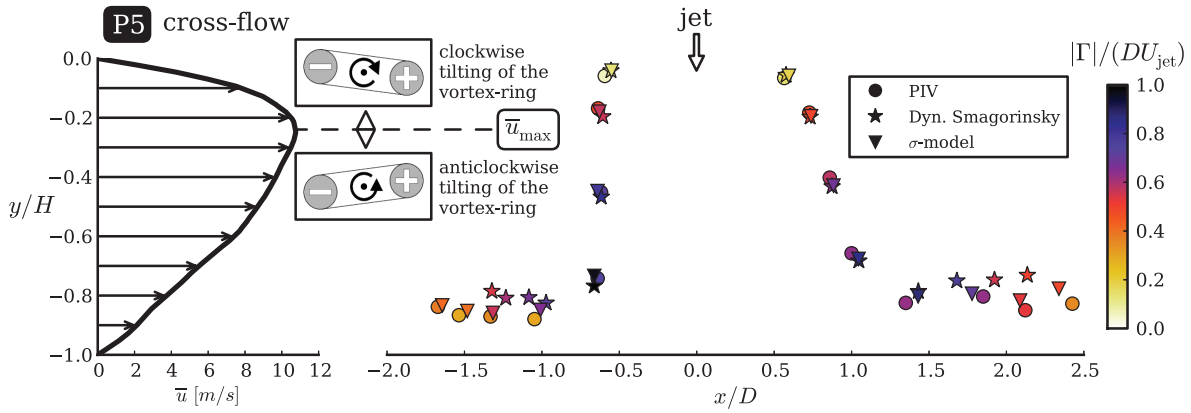

FIG. 24. Vortex core trajectories in plane P5 ($z = 0$) coloured by the absolute circulation of each vortex core normalised by the jet diameter, D, and the maximum jet velocity, $U_{\text{jet}} = 90\ m/s$. The mean cross-flow profile shown on the left corresponds to the LES with the dynamic Smagorinsky model at $x = -2D$, and allows to illustrate the interaction of the vortex-ring with the cross-flow. The two vortex cores have been tracked for $t = 0.6, 0.8, 1.0, 1.2, 1.4, 1.6, 1.8, 2.0\ ms$.

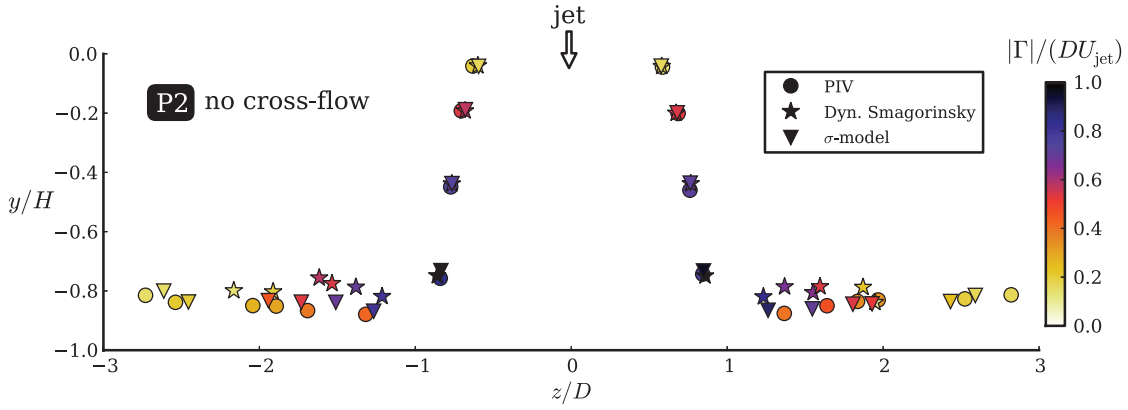

FIG. 25. Vortex core trajectories in plane P2 ($x = 0$) coloured by the absolute circulation of each vortex core normalised by the jet diameter, D, and the maximum jet velocity, $U_{\text{jet}} = 90\ m/s$. The two vortex cores have been tracked for $t = 0.6, 0.8, 1.0, 1.2, 1.4, 1.6, 1.8, 2.0, 3.0, 4.0\ ms$.

capture the vortex-ring tilting occurring in plane P5, the tilting direction depending on the position of the vortex-ring relatively to the location of the maximum streamwise velocity. The role of the SGS viscosity is relatively negligible during this phase since the vortex-ring behaves like a solid-rotation of fluid material, and the overall dissipation of kinetic energy, $-2(\nu + \nu_{\text{SGS}})S_{ij}S_{ij}$, is thus weakly sensitive to the value of the SGS viscosity. To illustrate this point, the squared magnitude of the resolved strain-rate tensor, $2S_{ij}S_{ij}$, is shown in

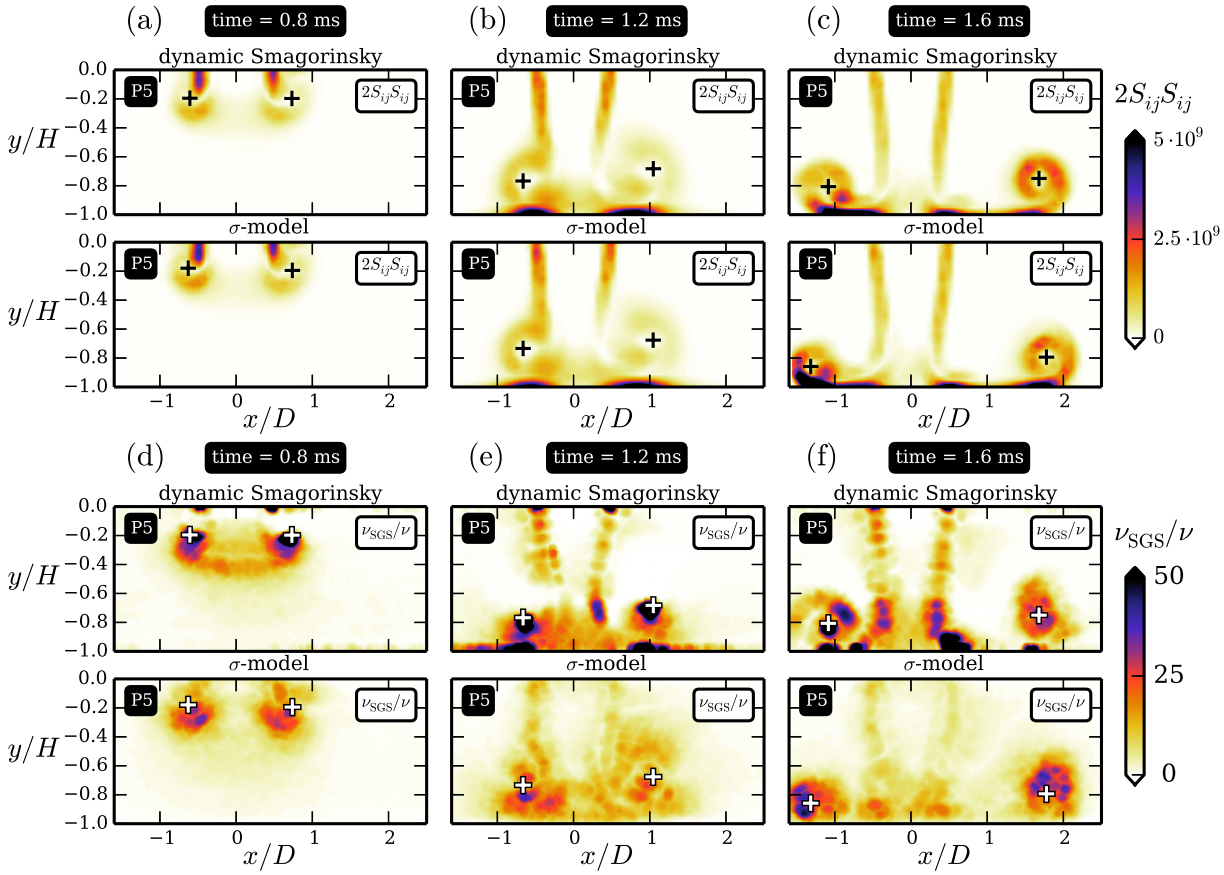

FIG. 26. Influence of the SGS viscosity model on the vortex-ring dynamics in plane P5 ($z = 0$). (a,b,c): squared magnitude of the resolved strain-rate tensor, $2S_{ij}S_{ij}$; (d,e,f): ratio of the SGS viscosity and the molecular viscosity, ν_{SGS}/ν. Black and white crosses indicate the location of the vortex-ring cores.

Fig. 26(a,b,c) and Fig. 27(a,b,c), and the SGS viscosity to molecular viscosity ratio, ν_{SGS}/ν, is presented in Fig. 26(d,e,f) and Fig. 27(d,e,f). When the vortex-ring travels towards the wall (Fig. 26(a) and Fig. 27(a)), the magnitude of the strain-rate tensor remains close to zero around the vortex cores, which hides any difference introduced by the use of a different SGS viscosity model.

After the impact ($t > 1.2\ ms$), the vortex-ring propagates along the plate and the first differences can be observed between the two SGS viscosity models. Generally speaking, the wall-propagation of a vortex in a cross-flow is governed by three phenomena: (1) the high strain-rate occurring between the vortex and the wall dissipates the vortex; (2) the cross-flow convects the vortex downstream (in the x-direction); (3) the cross-flow induces a

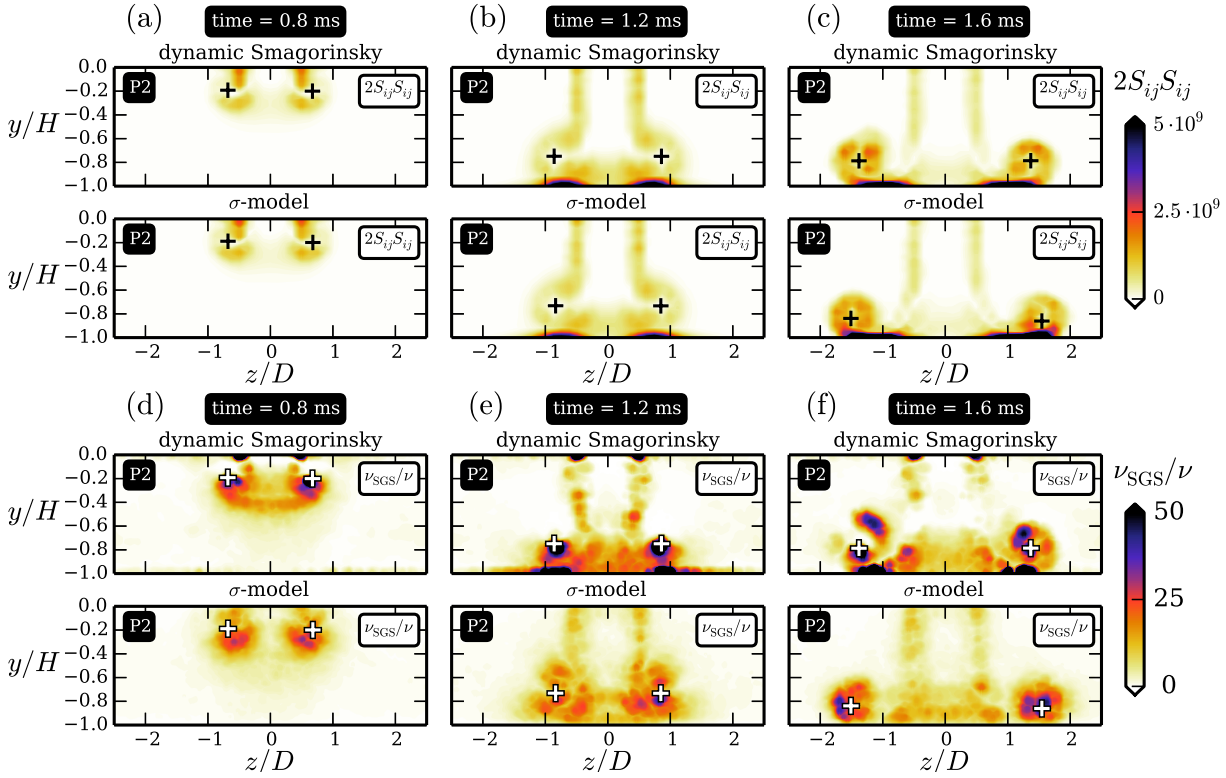

FIG. 27. Influence of the SGS viscosity model on the vortex-ring dynamics in plane P2 ($x = 0$). (a,b,c): squared magnitude of the resolved strain-rate tensor, $2S_{ij}S_{ij}$; (d,e,f): ratio of the SGS viscosity and the molecular viscosity, ν_{SGS}/ν. Black and white crosses indicate the location of the vortex-ring cores.

background vorticity which is favorable for the windward vortex, and cancels the vorticity of the lee side vortex. It is difficult to properly dissociate the influence of each effect, however, a possible scenario can be established looking at Fig. 24 and Fig. 25, for which the influence of the cross-flow can be isolated (phenomena (2) and (3)). In both planes, the vortex-ring stays further away from the wall with the dynamic Smagorinsky model. As shown in Fig. 26(e,f) and Fig. 27(e,f), this is most likely due to the SGS viscosity, which is higher with the dynamic Smagorinsky model because its time-scale operator is based on the strain-rate tensor magnitude, $\sqrt{2S_{ij}S_{ij}}$. Consequently, the effective viscosity of the flow $(\nu + \nu_{\mathrm{SGS}})$ increases, and prevents the penetration of the vortex-ring. This process is similar to the results obtained by Orlandi[64] (see Fig. 1 in Ref.[64]) and Walker *et al.*[65] (see Fig. 11 in Ref.[65]), who both observed that the rebound of the vortex depends on the Reynolds number, *i.e.* on the local effective viscosity of the fluid. Furthermore, this region of high

SGS viscosity also occurs where the strain-rate magnitude reaches its maximum values, *i.e.* between the vortex-ring and the wall (see Fig. 26(b,c) and Fig. 27(b,c)), which results in a high dissipation of the kinetic energy and slows down the vortex propagation. With the σ-model, the high magnitudes of the strain-rate tensor are balanced by the SGS viscosity which stays close to zero between the vortex-ring and the wall. Independently of the presence of the cross-flow, the SGS kinetic dissipation near the wall is thus negligible with the σ-model, which does not slow down the vortex-ring propagation more than expected. When the cross-flow is present, the vortex dynamics is additionally influenced by the phenomena (2) and (3), see Fig. 24. On the windward side, the convection velocity slows down the vortex propagation, and the background vorticity amplifies its circulation. On the lee side, the vortex propagation is enhanced by the cross-flow convection, and the background vorticity diminishes its circulation. The balance between the three phenomena not only becomes more complex, but the location of the vortex core also plays a crucial role. If the vortex core is located further away from the wall, the vortex is submitted to a stronger convection velocity (phenomenon (2)), and its circulation is more affected by the background vorticity (phenomenon (3)) since its size is less limited by the presence of the wall. Because the vortex cores stay further away from the wall with the dynamic Smagorinsky model, the balance between the three phenomena is completely different from the one occurring with the σ-model. It is notably interesting to note that the differences are less pronounced on the lee side propagation. First, because the vortex-ring is tilted at the impact which lifts the lee side vortex[60] and diminishes the influence of phenomenon (1). Second, because the vortex is located further away from the wall with the dynamic Smagorinsky model and thus submitted to a higher convection velocity, which compensates the slow down effect of the higher SGS dissipation.

The analysis of the vortex-ring dynamics reveals that the mitigated predictions of the dynamic Smagorinsky model are most likely due to the high values of the SGS viscosity in a region where no SGS dissipation is expected. This prevents the vortex penetration near the wall and slows down its propagation along the wall. To better understand this high dissipation predicted by the dynamic Smagorinsky model, it is important to recall some basics. The dynamic procedure was developed to make the SGS dissipation consistent with the structure of the resolved flow and the numerical discretisation. Near solid boundaries, it has the ability to accommodate the large values of the strain rate induced by the no-slip

condition in order to damp the SGS viscosity. In other words, the prediction quality of the dynamic Smagorinsky model relies on the ability of the dynamic constant to vanish near solid walls. Indeed, an asymptotic analysis near solid boundaries reveals that ν_{SGS} must be proportional to y^3, which implies that C_s^2 must be proportional to y^3 since $\sqrt{2S_{ij}S_{ij}}$ asymptotically tends to a constant near the wall[2,5]. It should be stressed that this y^3-behaviour corresponds to strong variations of C_s^2 in the near wall region which are not compatible with the formulation of the dynamic procedure. Indeed, the Germano-identity reads:

$$T_{ij} - \hat{\tau}_{ij} = L_{ij}, \tag{9}$$

where T_{ij} and τ_{ij} are respectively the SGS shear stress at the test and initial filter levels, and L_{ij} is the modified Leonard term. Introducing the constant C_s, Eq. 9 becomes:

$$C_s^2 \hat{\Delta}^2 \widehat{\mathcal{D}_s} \widehat{S_{ij}} - \Delta^2 (\widehat{C_s^2 \mathcal{D}_s S_{ij}}) = L_{ij}, \tag{10}$$

and C_s^2 from Eq. 10 is usually calculated with the assumption that it can be removed from the test filter in the second term of the left hand side of the equation. The desired near wall adaptation of the dynamic constant is thus somehow in contradiction with the hypothesis of taking the constant out of the test filter. Considering a mesh with a constant grid spacing, Δ_y^+, along the wall-normal direction, and assuming that C_s^2 follows its theoretical near wall behavior, $C_s^2 \propto y^{+3}$, one can evaluate the ratio of C_s^2 taken at two wall-normal locations separated by the grid spacing Δ_y^+:

$$\frac{C_s^2|_{y^+ + \Delta_y^+}}{C_s^2|_{y^+}} \sim \frac{\left(y^+ + \Delta_y^+\right)^3}{y^{+3}}, \tag{11}$$

and expanding Eq. 11 leads to:

$$\frac{C_s^2|_{y^+ + \Delta_y^+}}{C_s^2|_{y^+}} \sim 1 + 3\frac{\Delta_y^+}{y^+} + 3\left(\frac{\Delta_y^+}{y^+}\right)^2 + \left(\frac{\Delta_y^+}{y^+}\right)^3. \tag{12}$$

C_s^2 can be strictly removed from the test filter in Eq. 10 only if the ratio of Eq. 12 stays close to one. However, the last three terms in Eq. 12 are responsible for a systematic error, which is very high for the first layers of points close to the wall. Indeed, if the grid spacing is constant, the wall-normal distance can be described as a function of the number of points in the wall-normal direction such that Eq. 12 becomes:

$$\frac{C_s^2|_{y^+ + \Delta_y^+}}{C_s^2|_{y^+}} \sim 1 + \frac{3}{n} + \frac{3}{n^2} + \frac{1}{n^3}, \tag{13}$$

where n is the number of points in the wall-normal direction ($y^+ = n\Delta_y^+$). From Eq. 13, it appears that at the first off-wall grid point $\frac{C_s^2|_{y^+ + \Delta_y^+}}{C_s^2|_{y^+}} \sim 8$, which corresponds to a very high variation of the constant within the first cell. At the tenth off-wall grid point, the variation within the cell would still be around 30%. As a consequence, this contradiction between the desired damping of the dynamic constant near solid boundaries and the displacement of C_s^2 outside the test filter in Eq. 10 has a substantial effect over many layers of points parallel to the wall. Equation 13 shows that in the boundary layer, even with a good mesh refinement ($\Delta_y^+ \sim 5$ for industrial applications), there would be a large systematic error on the evaluation of the model constant that would not be sufficiently small to accommodate the large value of the strain-rate near the walls.

Other reasons could also explain the increase of the SGS dissipation with the dynamic Smagorinsky model in the regions where the flow should be dominated by viscous non-turbulent effects. The potential issues occurring in LES of industrial configurations is recalled hereafter.

- The stabilization procedure plays an important role. It generally involves a spatial averaging (in the present case a volume average as shown in Eq. 6), which assumes that the points used in the average procedure share the same model constant even if they do not have the same strain rate intensity. This average procedure helps stabilizing the calculation but also affects the ability of the dynamic procedure to dampen the turbulent viscosity near solid boundaries. In the pulsatile jet in cross-flow configuration, this is especially true during the impingement of the vortex-ring because there are no homogeneous directions. Consequently, the stabilization procedure (volume averaging in the present case) probably leads to a wrong estimation of the final SGS viscosity.

- The evaluation of the dynamic constant depends on the mesh refinement. When the velocity gradient increases at the wall, and thus the friction velocity, the non-dimensional grid spacing, Δ_y^+, increases and leads to a less accurate prediction of the dynamic constant, and the overall SGS viscosity no longer compensates the large values of the strain rate.

- A systematic clipping of the negative values of C_s^2 is usually employed because the dynamic procedure is ill-posed and leads to large variations of the model constant (see

Eq. 6). If those negative values were kept, it would decrease the overall value of the SGS viscosity[66] but could also affect the numerical stability of the solver.

The σ-model does not suffer from these potential issues. The fully local definition of the time-scale operator (no explicit filtering or space-averaging required) is so that it automatically vanishes near solid boundaries as long as there are enough nodes to discretise the boundary layer. As a consequence, the viscosity level remains very low in the vicinity of the wall, even when the strain-rate tensor reaches very high magnitudes.

VI. CONCLUSIONS

An experimental database of a pulsatile impinging jet in a turbulent cross-flow was presented in this paper. The experiment was designed so that a large-eddy simulation of the same configuration could be performed. The velocity components were measured thanks to the PIV technique, which provided a precise characterization of the boundary conditions to be used for the numerical simulations. First, some preliminary tests showed the moderate impact of the numerical scheme. Then, two SGS viscosity models were tested: the dynamic Smagorinsky model[1] (with a local formulation of the constant and the clipping of the negative values), and the σ-model[2]. The performances of both SGS models were assessed by comparing the LES results to the PIV measurements in different planes.

The differences between the two SGS models appeared when the vortex-ring was interacting with the surface of impact. During this phase, the propagation velocity of the vortex-ring was under-estimated by the dynamic Smagorinsky model. An analysis involving the vortex core trajectories, the SGS viscosity, and the squared magnitude of the strain-rate tensor, revealed that the dynamic constant was no longer able to accommodate the high values of the strain-rate near the wall, which slows down the vortex propagation. The mitigated predictions of the dynamic Smagorinsky model were explained by different factors: the loss of homogeneous directions during the vortex-ring impact, the dependence of the dynamic procedure on the mesh resolution, and the systematic clipping leading to an over-estimation of the total SGS dissipation. At the same time, the σ-model led to a better prediction of the vortex-ring propagation because it is based on the singular values of the velocity gradient tensor, which naturally vanished at the wall.

The conclusions are expected to hold in complex geometries such as IC engines, where the confinement of the flow enhances the influence of the solid boundaries, and where the boundary layers are rarely homogeneous. The PIV results, as well as the geometry and the mesh used for the LES, are made available to the community upon request to the authors.

ACKNOWLEDGMENTS

The authors gratefully acknowledge CINES for giving access to super-computing facilities. Damien Peyresaubes, Thomas Collazo, Jerome Cherel and Nicolas Gautreau are also thanked for their contributions during the setting up of the test bench and for performing the experiments. The authors would also like to thank Dr. John Elsnab for his helpful comments about the vortex-ring dynamics. Some of the results presented in this paper were obtained during the 2010 Center for Turbulence Research summer program at Stanford University; Prof. P. Moin and Prof. H. Choi are warmly acknowledged for fruitful discussions during the course of this program.

REFERENCES

[1]M. Germano, U. Piomelli, P. Moin, and W. Cabot. A dynamic subgrid-scale eddy viscosity model. *Phys. A*, 3(7):1760–1765, July 1991.

[2]F. Nicoud, H. B. Toda, O. Cabrit, S. Bose, and J. Lee. Using singular values to build a subgrid-scale model for large eddy simulations. *Phys.*, 23(8):085106, 2011.

[3]J. Smagorinsky. General circulation experiments with the primitive equations: 1. the basic experiment. *Mon. Weather Rev.*, 91(3):99–164, 1963.

[4]O. Métais and M. Lesieur. Spectral large-eddy simulation of isotropic and stably stratified turbulence. *J. Fluid Mech.*, 239:157–194, 1992.

[5]F. Nicoud and F. Ducros. Subgrid-scale stress modelling based on the square of the velocity gradient tensor. *Flow, Turb. and Combustion*, 62:183–200, 1999.

[6]A. W. Vreman. An eddy-viscosity subgrid-scale model for turbulent shear flow: algebraic theory and applications. *Phys.*, 16(10):3670–3681, 2004.

[7]G. Bruneaux. Combustion structure of free and wall-impinging diesel jets by simultaneous laser-induced fluorescence of formaldehyde, poly-aromatic hydrocarbons, and hydrooxides. *Int. J. Engine Research*, 9:249–265, 2008.

[8]S. Ghosal, T. S. Lund, P. Moin, and K. Akselvoll. A dynamic localization model for large-eddy simulation of turbulent flows. *J. Fluid Mech.*, 286:229–255, 1995.

[9]C. Meneveau, T. S. Lund, and W. H. Cabot. A lagrangian dynamic subgrid-scale model of turbulence. *J. Fluid Mech.*, 319:353–385, 1996.

[10]N. Park and K. Mahesh. Reduction of the Germano-identity error in the dynamic Smagorinsky model. *Phys.*, 21(6):065106, 2009.

[11]G. Comte-Bellot and S. Corrsin. Simple Eulerian time correlation of full-and narrow-band velocity signals in grid-generated, 'isotropic' turbulence. *J. Fluid Mech.*, 48(2):273–337, 1971.

[12]H. S. Kang, S. Chester, and C. Meneveau. Decaying turbulence in an active-grid-generated flow and comparisons with large-eddy simulation. *J. Fluid Mech.*, 480:129–160, 2003.

[13]P. Moin and J. Kim. Numerical investigation of turbulent channel flow. *J. Fluid Mech.*, 118:341–377, 1982.

[14]J. Kim, P. Moin, and R. Moser. Turbulence statistics in fully developed channel flow at low Reynolds number. *J. Fluid Mech.*, 177:133–166, 1987.

[15]R. D. Moser, J. Kim, and N. N. Mansour. Direct numerical simulation of turbulent channel flow up to $Re_\tau = 590$. *Phys.*, 11(4):943–945, 1999.

[16]T. Voelkl, D. I. Pullin, and D. C. Chan. A physical-space version of the stretched-vortex subgrid-stress model for large-eddy simulation. *Phys.*, 12(7):1810–1824, 2000.

[17]J. Gullbrand and F. K. Chow. The effect of numerical errors of turbulence models in large-eddy simulations of channel flow, with and without explicit filtering. *J. Fluid Mech.*, 495:323–341, 2003.

[18]G. Cui, H. Zhou, Z. Zhang, and L. Shao. A new dynamic subgrid eddy viscosity model with application to turbulent channel flow. *Phys.*, 16(8):2835–2842, August 2004.

[19]J. Meyers and P. Sagaut. Is plane-channel flow a friendly case for the testing of large-eddy simulation subgrid-scale models? *Phys.*, 19(4):048105, 2007.

[20]E. Lévêque, F. Toschi, L. Shao, and J.-P. Bertoglio. Shear-improved Smagorinsky model for large-eddy simulation of wall-bounded turbulent flows. *J. Fluid Mech.*, 570:491–502, 2007.

[21]S. Stolz, P. Schlatter, and L. Kleiser. High-pass filtered eddy-viscosity models for large-eddy simulations of transitional and turbulent flow. *Phys.*, 17(6):065103, 2005.

[22]S. T. Bose, P. Moin, and D. You. Grid-independent large-eddy simulation using explicit filtering. *Phys.*, 22(10):105103, 2010.

[23]S.R. Ahmed and G. Ramm. Some salient features of the time-averaged ground vehicle wake. *SAE-paper*, 840300, 1984.

[24]Y. Zang, R. L. Street, and J. R. Koseff. A dynamic mixed subgrid-scale model and its application to turbulent recirculating flows. *Phys. A*, 5(12):3186–3196, 1993.

[25]K.-S. Yang and J. H. Ferziger. Large-eddy simulation of turbulent obstacle flow using a dynamic subgrid-scale model. *AIAA J.*, 31(8):1406–1413, 1993.

[26]H. S. Kang and C. Meneveau. Effect of large-scale coherent structures on subgrid-scale stress and strain-rate eigenvector alignments in turbulent shear flow. *Phys.*, 17(5):055103, 2005.

[27]B. Enaux, V. Granet, O. Vermorel, C. Lacour, L. Thobois, V. Dugué, and T. Poinsot. Large eddy simulation of a motored single-cylinder piston engine: Numerical strategies and validation. *Flow, Turb. and Combustion*, 86:153–177, 2011.

[28]N. Didden. On the formation of vortex rings: rolling-up and production of circulation. *Z. Angew. Math. Phys.*, 30(1):101–116, 1979.

[29]M. Nitsche and R. Krasny. A numerical study of vortex ring formation at the edge of a circular tube. *J. Fluid Mech.*, 276:139–161, 1994.

[30]T. T. Lim and T. B. Nickels. Vortex rings. In *Fluid vortices*, pages 95–153. Springer, 1995.

[31]P. Sagaut, E. Garnier, and N. Adams. *Large eddy simulation for compressible flows.* Springer Science Science + Business Media B. V., 2009.

[32]J. H. Bell and P. Bradshaw. Boundary-layer predictions for small low-speed contractions. *AIAA J.*, 27:372–374, 1989.

[33]D. Brassard and M. Ferchichi. Transformation of a polynomial for a contraction wall profile. *J. Fluids Eng.*, 127(1):183–185, 2005.

[34]R. D. Mehta and P. Bradshaw. Design rules for small low speed wind tunnels. *The aeronautical Journal of the Royal Aeronautical Society*, November, 1979.

[35]R. D. Mehta. Turbulent boundary layer perturbed by a screen. *AIAA J.*, 23(9):1335–1342, 1985.

[36]L. Hesselink. Digital image processing in flow visualization. *Annu. Rev. Fluid Mech.*, 20:421–486, 1988.

[37]J. Westerweel. Theoretical analysis of the measurement precision in particle image velocimetry. *Exp. Fluids*, 29(1):S003–S012, 2000.

[38]O. Colin and M. Rudgyard. Development of high-order Taylor-Galerkin schemes for unsteady calculations. *J. Comput. Phys.*, 162(2):338–371, 2000.

[39]V. Moureau, G. Lartigue, Y. Sommerer, C. Angelberger, O. Colin, and T. Poinsot. Numerical methods for unsteady compressible multi-component reacting flows on fixed and moving grids. *J. Comput. Phys.*, 202(2):710–736, 2005.

[40]O. Cabrit and F. Nicoud. Direct simulations for wall modeling of multicomponent reacting compressible turbulent flows. *Phys.*, 21(5):055108, 2009.

[41]H. B. Toda, O. Cabrit, G. Balarac, S. Bose, J. Lee, H. Choi, and F. Nicoud. A subgrid-scale model based on singular values for LES in complex geometries. In NASA Ames/Stanford Univ. Center for Turbulence Research, editor, *Proc. of the Summer Programm*, pages 193–202, 2010.

[42]D. K. Lilly. A proposed modification of the Germano subgrid-scale closure mmethod. *Phys. A*, 4(3):633–635, 1992.

[43]R. B. Dean. Reynolds number dependence of skin friction and other bulk flow variables in two-dimensional rectangular duct flow. *J. Fluids Eng.*, 100(2):215–223, 1978.

[44]S. Mendez and F. Nicoud. Large-eddy simulation of a bi-periodic turbulent flow with effusion. *J. Fluid Mech.*, 598:27–65, 2008.

[45]O. Cabrit and F. Nicoud. Direct numerical simulation of a reacting turbulent channel flow with thermochemical ablation. *J. Turb.*, 11(44):1–33, 2010.

[46]T. J. Poinsot and S. K. Lele. Boundary conditions for direct simulations of compressible viscous flows. *J. Comput. Phys.*, 101(1):104–129, 1992.

[47]M. Baum, T. J. Poinsot, and D. Thévenin. Accurate boundary conditions for multicomponent reacting flows. *J. Comput. Phys.*, 116(2):247–261, 1995.

[48]C. S. Yoo and H. G. Im. Characteristic boundary conditions for simulations of compressible reacting flows with multi-dimensional, viscous and reacting effects. *Comb. Theory and Modelling*, 11(2):259–286, April 2007.

[49]G. Lodato, P. Domingo, and L. Vervisch. Three-dimensional boundary conditions for direct and large-eddy simulation of compressible viscous flows. *J. Comput. Phys.*, 227(10):5105–5143, 2008.

[50]V. Granet, O. Vermorel, T. Leonard, L. Gicquel, and T. Poinsot. Comparison of nonreflecting outlet boundary conditions for compressible solvers on unstructured grids. *AIAA J.*, 48(10):2348–2364, 2010.

[51]F. Jaegle, O. Cabrit, S. Mendez, and T. Poinsot. Implementation methods of wall functions in cell-vertex numerical solvers. *Flow, Turb. and Combustion*, 85(2):245–272, September 2010.

[52]T. Poinsot and D. Veynante. *Theoretical and Numerical Combustion*. R.T. Edwards, 2005.

[53]N. Guezennec and T. Poinsot. Acoustically nonreflecting and reflecting boundary conditions for vorticity injection in compressible solvers. *AIAA J.*, 47(7):1709–1722, 2009.

[54]A. Smirnov, S. Shi, and I. Celik. Random flow generation technique for large eddy simulations and particle-dynamics modelling. *J. Fluids Eng.*, 123(2):359–371, 2001.

[55]T. J. R. Hughes. *The finite element method: linear static and dynamic finite element analysis*. Prentice-Hall, Inc., 1987.

[56]P. D. Lax and B. Wendroff. Systems of conservation laws. *Commun. Pure Appl. Math.*, 13(2):217–237, 1960.

[57]P. D. Lax and B. Wendroff. Difference schemes for hyperbolic equations with high order of accuracy. *Commun. Pure Appl. Math.*, 17(3):381–398, 1964.

[58]P. I. Crumpton, J. A. Mackenzie, and K. W. Morton. Cell vertex algorithms for the

compressible Navier-Stokes equations. *J. Comput. Phys.*, 109(1):1–15, November 1993.

[59]L. Selle, G. Lartigue, T. Poinsot, R. Koch, K.-U. Schildmacher, W. Krebs, B. Prade, P. Kaufman, and D. Veynante. Compressible large eddy simulation of turbulent combustion in complex geometry on unstructured meshes. *Comb. Flame*, 137(4):489–505, 2004.

[60]L. D. Couch and P. S. Krueger. Experimental investigation of vortex rings impinging on inclined surfaces. *Exp. Fluids*, 51(4):1123–1138, October 2011.

[61]C. C. Chu, C. T. Zang, C. C. Chang, R. Y. Chang and W. T. Chang. Heads-on collision of two coaxial vortex rings: experiment and computation. *J. Fluid Mech.*, 296:39–71, 1995.

[62]T. T. Lim, K. B. Lua, and K. Thet. Does Kutta lift exist on a vortex ring in a uniform cross flow? *Phys.*, 20(5):051701, May 2008.

[63]M. Cheng, J. Lou, and T. T. Lim. Motion of a vortex ring in a simple shear flow. *Phys.*, 21(8):081701, August 2009.

[64]P. Orlandi. Vortex dipole rebound from a wall. *Phys. A*, 2(8):1429–1436, 1990.

[65]J. D. A. Walker, C. R. Smith, A. W. Cerra, and T. L. Doligalski. The impact of a vortex ring on a wall. *J. Fluid Mech.*, 181:99–140, 1987.

[66]U. Piomelli, W. H. Cabot, P. Moin, and S. Lee. Subgrid-scale backscatter in turbulent and transitional flows. *Phys. A*, 3(7):1766–1771, 1991.